Title	A kinetic study on oxygen isotopic evolution of primitive amorphous silicate dust and refractory inclusions in the early Solar System
Author(s)	山本, 大貴
Citation	北海道大学. 博士(理学) 甲第13578号
Issue Date	2019-03-25
DOI	10.14943/doctoral.k13578
Doc URL	http://hdl.handle.net/2115/77016
Type	theses (doctoral)
File Information	Daiki_Yamamoto.pdf

A kinetic study on oxygen isotopic evolution of primitive amorphous silicate dust and refractory inclusions in the early Solar System

(初期太陽系における始原的非晶質ケイ酸塩ダストと難揮発性包有物の酸素同位体進化の速度論的研究)

A dissertation submitted for the doctoral degree of science

Presented by
Daiki Yamamoto

Department of Natural History Sciences
Graduate School of Science
Hokkaido University

March, 2019

Contents

Abstract

Oxygen is one of the most abundant elements in the Solar System, and oxygen isotopic compositions of extraterrestrial materials could be a good tracer for various chemical and physical processes involving solid, liquid, and gas phases in the early Solar System. The oxygen isotopic compositions of primitive extraterrestrial materials show the mass-independent oxygen isotopic variation, which is an evidence of isotopic mixing/exchange between ^{16}O-rich and ^{16}O-poor reservoirs in the early Solar System. The Genesis mission discovered that oxygen isotopic composition of the Sun is ^{16}O-rich, suggesting that primitive materials in the Solar System was initially ^{16}O-rich and observed isotopic variation in extraterrestrial materials was produced through oxygen isotopic exchange with isotopically distinct disk gas. Amorphous silicate dust and calcium-aluminum-rich inclusions (CAIs) are recognized as primitive components in the Solar System, and they should record the evolution of the protosolar disk as variation of their oxygen isotopic compositions. In this thesis, I experimentally investigated oxygen isotopic exchange kinetics of amorphous silicate dust with forsterite and enstatite compositions (chapter 2) and CAI melt (chapter 3) with disk water vapor by conducting a series of experiments using their synthetic analogues at protosolar disk-like low pressures of water vapor to investigate oxygen isotopic evolution of primitive materials in the early Solar System. This thesis consists of mainly two parts as follows;

Oxygen isotopic exchange between amorphous silicates and water vapor and its implications to oxygen isotopic evolution in the early Solar System: I conducted a series of oxygen isotopic exchange experiments between submicron-sized amorphous silicate dust with forsterite and enstaite compositions and water vapor at 803–1123 K and water vapor pressure (P_{H2O}) of 10^{-2} and 0.3 Pa. At $P_{\mathrm{H2O}} = 0.3$ Pa, oxygen isotopic exchange reaction is controlled by diffusive isotopic exchange in the amorphous structure with the diffusive isotopic exchange rates of D (m^2 s^{-1}) = $(1.5 \pm 1.0) \times 10^{-19} \exp[-161.5 \pm 14.1 \text{ (kJ mol}^{-1}) R^{-1} (1/T-1/1200)]$ for amorphous forsterite

and D (m^2 sec^{-1}) = $(5.0 \pm 0.2) \times 10^{-21}$ exp[-161.3 ± 1.5 (kJ mol^{-1}) R^{-1} $(1/T - 1/1200)$] for amorphous enstatite. At $P_{H2O} = 0.01$ Pa, the isotopic exchange reaction for amorphous forsterite is controlled by a supply of water vapor, and the supply-controlled isotopic exchange rate was evaluated. Application of kinetic data to the protosolar disk conditions indicates that original oxygen isotopic signatures of amorphous silicate dust would be eliminated within the disk gas lifetime if the dust was kept at temperatures above ~500–650 K. Most extraterrestrial silicate samples available in the laboratories (e.g. chondrules, chondrite matrix, interplanetary dust particles, and cometary silicate dust) are ^{16}O-poor isotopic compositions, suggesting that most of primitive silicate dust would have been thermally processed at temperatures above ~500–650 K in a H_2O-enriched environment in the early Solar System.

Oxygen isotopic exchange kinetics between CAI melt and water vapor: The oxygen isotopic exchange experiments between silicate melt with a type B CAI-like composition and ^{18}O-enriched water vapor at a disk-like low P_{H2O} of 5×10^{-2} Pa were carried out at 1390°C. The heated samples were composed of melt and spinel. The ^{18}O fraction gradually decreased from the surface to the interior of the droplet, and that at the surface increased with time, suggesting that the surface isotope exchange and the volume diffusion of oxygen occurred simultaneously. The oxygen isotopic profiles were explained by a three-dimensional spherical diffusion equation with a time-dependent surface concentration, yielding the oxygen diffusion coefficient of $\sim 1.87 \times 10^{-7}$ cm^2 sec^{-1} and the surface oxygen isotopic exchange efficiency of ~0.27 for colliding water molecules. According to the kinetics for oxygen isotopic exchange in the protosolar disk, homogeneous oxygen isotopic compositions of melilite in most natural Type B CAIs are explained by heating of CAI melts for at least a dozen days above the melilite liquidus during the type B CAI formation in the early Solar System.

Chapter 1

1. General Introduction

1.1 *Oxygen isotopic evolution of primitive materials in the Solar System*

Oxygen is one of the most abundant elements in the Solar System and could be present in the forms of silicate, oxide, ice, and gas (H_2O and CO) in the early Solar System. It has received much attention in the filed of cosmochemistry since the first discovery of oxygen isotopic anomalies in Allende refractory inclusions (Clayton et al., 1973). Since then, it has been found that there are oxygen isotopic variations among extraterrestrial materials. Oxygen has three stable oxygen isotopes; ^{16}O, ^{17}O, and ^{18}O. Oxygen isotopic fractionations are expressed as permil deviation from the Standard Mean Ocean Water (SMOW); $\delta^{17,18}\mathrm{O} = [(^{17,18}\mathrm{O}/^{16}\mathrm{O})_{\mathrm{sample}}/(^{17,18}\mathrm{O}/^{16}\mathrm{O})_{\mathrm{SMOW}}-1] \times 1000$ (‰). On the three oxygen isotopic diagram, δ^{18}O (‰) versus δ^{17}O (‰), oxygen isotopic compositions of terrestrial materials are plotted along the mass-dependent terrestrial fractionation (TF) line associated with chemical and/or physical processes, while oxygen isotopic compositions of primitive extraterrestrial materials are not plotted on the TF line and have their own characteristic oxygen isotopic compositions (mass independent fractionation). The mass-independent fractionation of primitive extraterrestrial materials is considered to be a result of mixing between ^{16}O-rich and ^{16}O-poor reservoirs. The Genesis spacecraft that captured Solar wind particles discovered that the oxygen isotopic compositions of the Sun is enriched in ^{16}O compared with most extraterrestrial materials, but similar to spinel in CAIs and amoeboid olivine aggregates from unmetamorphoused chondrites (Yurimoto et al., 1998; McKeegan al., 2011; Fagan et al., 2004; Kawasaki et al., 2018). This indicates that primitive Solar System materials would have initially Sun-like ^{16}O-rich oxygen isotopic compositions. On the other hand, the ^{16}O-poor reservoir may have been formed as H_2O through self-shielding of carbon monoxide (CO) during isotopically selective photodissociation in the protosolar molecular cloud and/or the protosolar disk (Yurimoto & Kuramoto, 2004; Lyons and Young, 2005); CO molecules with minor oxygen isotopes ($C^{17}O$ and $C^{18}O$) are dissociated by UV photolysis in the deeper interior from the surface of the protosolar molecular cloud and/or the protosolar disk, while the most abundant $C^{16}O$ is not due to self-shielding, resulting in the formation of ^{16}O-poor H_2O through hydrogenation (Yurimoto & Kuramoto, 2004; Lyons and Young, 2005). The evidence of the presence of ^{16}O-poor reservoir was found in the ^{16}O-poor isotopic compositions of cosmic symplectites found in Acfer 094 ungrouped carbonaceous chondrite (Sakamoto et al., 2007; Seto et al., 2008; Abe et al., 2017) and the comet 81P/Wild2 (Nguyen et al., 2017). The cosmic symplectites are considered to have formed through oxidation and sulfidation of Fe-Ni metal with H_2O and H_2S (Sakamoto et al., 2007; Seto et al., 2008). Therefore, the oxygen isotopic exchange between ^{16}O-rich primitive materials and ^{16}O-poor water vapor is thus a key process for oxygen isotopic evolution of extraterrestrial materials in the early evolution stage of protosolar disk.

Amorphous silicate dust and calcium-aluminum-rich refractory inclusions (CAIs) are present during the early epoch of the Solar System evolution, and these objects are recognized as primitive materials in the Solar System. The variation of oxygen isotopic compositions of these materials would reflect the degree of oxygen isotopic exchange reaction. Because the exchange rate depends on the physicochemical conditions of the protosolar disk (e.g., temperature, pressure), oxygen isotopic compositions of these extraterrestrial materials could be a good tracer for the disk physicochemical conditions. However, because of the lack of quantitative data on oxygen isotopic exchange kinetics between primitive extraterrestrial materials and water vapor, the disk conditions cannot be inferred from oxygen isotopic compositions of primitive extraterrestrial materials in spite of the extensive studies on oxygen isotopic measurements of natural samples.

1.2 *Aims and outlines of this thesis*

In this thesis, I experimentally investigated oxygen isotopic exchange kinetics of amorphous silicate dust and CAI melt with disk water vapor by conducting a series of experiments using their synthetic analogues at protosolar disk-like low pressures of water vapor. Chapter 2 focused on oxygen isotopic exchange kinetics between amorphous silicate dust with forsterite and enstatite compositions and water vapor in order to constrain disk thermal conditions, where original oxygen isotopic signatures of primitive silicate dust were preserved or erased. Chapter 3 focused on oxygen isotopic exchange kinetics between CAI melt and water vapor in order to investigate the thermal history of CAIs in the earliest Solar System. The summary of this thesis and future works are described in chapter 4.

Chapter 2

2. Oxygen isotopic exchange between amorphous silicates and water vapor and its implications to oxygen isotopic evolution in the early Solar System

2.1 *Introduction*

Silicate dust is the primitive building block of solid materials in the Solar System, and oxygen isotopic exchange between silicate dust and disk gas may have played a key role in oxygen isotopic evolution of solid materials during the early stage of the Solar System formation. Primitive silicate dust would initially have Sun-like ^{16}O-rich oxygen isotopic compositions and evolve to ^{16}O-poor compositions through isotopic exchange with ^{16}O-poor water vapor in the protosolar disk (chapter 1). The dominant solid component in the early evolution stage of protoplanetary disk would be amorphous silicate dust (e.g., Nuth et al., 2005). The observation of more crystalline silicate dust in the inner part of protoplanetary disks than in the outer part (van Boekel et al. 2005; Ratzka et al. 2007) suggests that thermal annealing of pristine amorphous silicate dust occurs in protoplanetary disks. Therefore, the oxygen isotopic exchange between primitive amorphous silicate dust and water vapor would occur during the thermal annealing in the early Solar System, and contribute to the oxygen isotopic evolution of early Solar System materials.

Thermal annealing of amorphous silicate dust in protoplanetary disks is thus important to understand the early chemical evolution of disks and the Solar System, but little has been known about the oxygen isotopic exchange reaction between amorphous silicates and water vapor under disk-like low-pressure conditions. It has been widely accepted that silicate dust with pyroxene and olivine compositions exist as major circumstellar silicate dust (Waters et al., 1996; Henning, 2010 and references therein). Therefore, this study focuses on kinetics of oxygen isotope exchange between amorphous silicate with forsterite and enstatite compositions and water vapor, and performed the isotopic exchange experiments under disk-like low-pressure conditions.

2.2 *Experiments and analysis*

Oxygen Isotopic Exchange Experiments

The oxygen isotope exchange experiments between submicron-sized amorphous silicate dust with forsterite and enstatite compositions (called as amorphous forsterite and amorphous enstatite hereafter) and ^{18}O-enriched water vapor were carried out at 803−1073 K under disk-like water vapor pressure of $P_{\mathrm{H2O}} = 0.01$ and 0.3 Pa using a gold-mirror vacuum furnace (Thermo-Riko GFA 430VN; Fig. 2.1). The furnace consists of a silica glass tube (36 mm in diameter and 450 mm in length) surrounded by an Inconel alloy coil heater and a gold-coated mirror tube, a pumping system (a turbo-molecular pump and a scroll pump; HiCube 80 Eco, Pfeiffer Vacuum), and gas inlets for $H_2{}^{16}O$ and $H_2{}^{18}O$ vapor. The pressure inside the furnace was measured with a Pirani/cold-cathode gauge (Pfeiffer PKR251) using a proper conversion factor for water

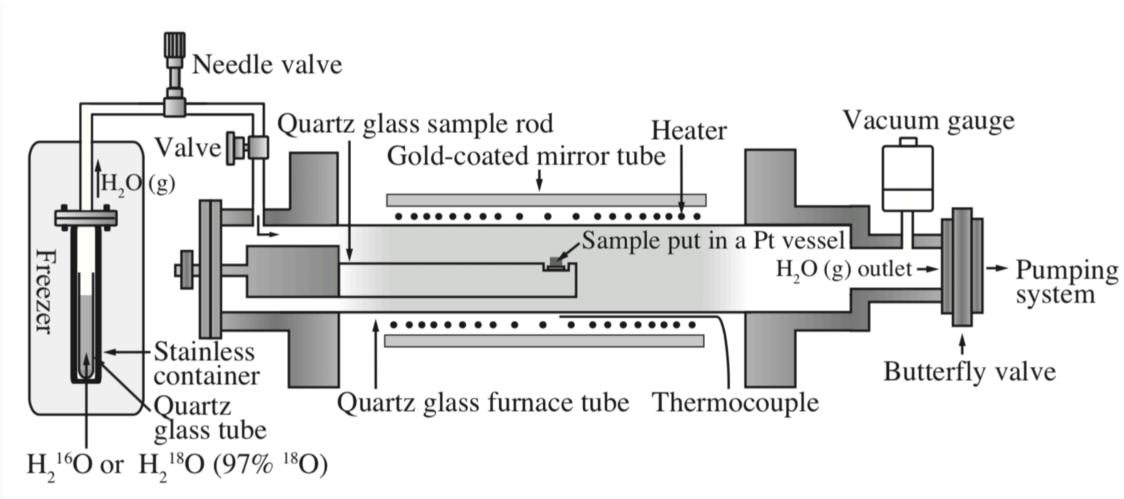

Fig. 2.1. A schematic illustration of the vacuum furnace configuration.

vapor.

The furnace temperature was measured and controlled by a type K thermocouple outside of the silica glass tube. The sample temperature in the furnace was calibrated using melting points of sodium chloride (800.4°C), potassium bromide (730°C), lithium bromide (547°C), and indium (156.6°C) placed at the same location as the sample inside the furnace (Yamamoto and Tachibana, 2018). The temperature calibration was made both at P_{H2O} = 500 Pa and in vacuum (10^{-4}–10^{-5}Pa). No significant pressure dependence of temperature calibration between P_{H2O} = 500 Pa and in vacuum was found, and a single interpolated regression line for the temperature correction was applied to heat the samples at desired temperatures under all P_{H2O} conditions. The uncertainty of the sample temperature was ± 5°C.

Submicron-sized amorphous forsterite and enstatite grains, synthesized by an induced thermal plasma method (Koike et al. 2010; Imai, 2012), were used as a starting material for the experiments. The amorphous powder was synthesized by vaporizing starting materials ($Mg(OH)_2$ and SiO_2 with the Mg/Si ratios of 2 and 1 for amorphous forsterite and enstatite, respectively) in high temperature plasma (~10^4 K), followed by quenching (Koike et al. 2010; Imai et al., 2012). The amorphous powder has a spherical shape with average diameters of 80 nm and 70 nm for amorphous forsterite and enstatite, respectively (Koike et al. 2010; Imai, 2012). A part of the amorphous forsterite grains was annealed at 1073 K for 24 hours in air to obtain crystalline forsterite without severe sintering (Koike et al. 2010), which were used as a reference of isotopically-normal crystalline forsterite. About 30 mg of the starting material was used for each experiment. The powder was put in a platinum vessel, and placed in a silica glass sample stand in the furnace.

Liquid reagent of $H_2{}^{18}O$ (97-atom% ^{18}O; Sigma-Aldrich) put in a silica glass container was sealed into a stainless container in a nitrogen-purged glove box to eliminate the contribution of $H_2{}^{16}O$ from the ambient gas. Liquid $H_2{}^{18}O$ in the stainless container was frozen in a freezer, and the stainless container was then connected to the gold-mirror vacuum furnace through a gas flow line. The temperature of $H_2{}^{18}O$ was kept at 253 K and 243 K for the experiments at P_{H2O} of 0.3 and 0.01 Pa. The gas species in the furnace was monitored by a quadrupole mass spectrometer (QMS; HORIBASTC QL-SG01-065-1A). The most dominant gas species was $H_2{}^{18}O$, and the detected $H_2{}^{16}O/H_2{}^{18}O$ ratio was consistent with $^{16}O/^{18}O$ of the reagent $H_2{}^{18}O$ (97-atom% ^{18}O).

A flow rate of $H_2{}^{18}O$ vapor was adjusted by a needle valve and a gas evacuation rate was adjusted by a butterfly valve attached to the pumping system. The balance between both the gas flow and evacuation rates determined the P_{H2O} in the furnace. After P_{H2O} stabilized at the room temperature, the sample was heated up from the room temperature to a desired temperature (803−1123 K) in 20 minutes. Then, the sample was kept at the temperature for a desired duration (0−448 hours), and was cooled down to the room temperature in ~20 minutes. The P_{H2O} was stable in most runs, but occasionally adjusted during experiments if necessary. I also conducted annealing experiments at P_{H2O} of 0.3 Pa using isotopically-normal (i.e. ^{16}O-dominant) water for comparison. The experimental conditions are listed in Tables 2.1, 2.2, and 2.3.

Table 2.1. Experimental conditions and results for amorphous forsterite annealed with $H_2{}^{16}O$ and $H_2{}^{18}O$ vapor of 0.3 and 0.01 Pa at 803−883 K. Errors represent the 1σ standard deviations of the means.

Temperature (K)	P_{H2O} (Pa)	Duration (hr)	Gas	Peak position (cm^{-1})[a]	$\Delta\kappa/\kappa_0$ (%)	$f^{18}O$ (IR)[b]	$f^{18}O$ (SIMS)[c]
883	0.3	4	$H_2{}^{18}O$	970.74 ± 0.83	1.05 ± 0.09	/	0.19 ± 0.003
883	0.3	6	$H_2{}^{18}O$	967.49 ± 1.73	1.38 ± 0.18	/	0.30 ± 0.018
883	0.3	8	$H_2{}^{18}O$	963.87 ± 0.61	1.75 ± 0.07	/	/
883	0.3	24	$H_2{}^{18}O$	961.94 ± 0.82	1.94 ± 0.09	/	0.47 ± 0.009
883	0.3	48	$H_2{}^{18}O$	crystallized	/	/	/
883	0.3	72	$H_2{}^{18}O$	crystallized	/	/	/
883	0.01	0	$H_2{}^{18}O$	979.28 ± 1.04	0.18 ± 0.11	0.04 ± 0.025	/
883	0.01	4	$H_2{}^{18}O$	977.13 ± 1.49	0.40 ± 0.16	0.08 ± 0.034	/
883	0.01	4	$H_2{}^{18}O$	977.97 ± 1.28	0.31 ± 0.14	0.07 ± 0.030	/
883	0.01	8	$H_2{}^{18}O$	975.27 ± 1.69	0.58 ± 0.18	0.12 ± 0.039	/
883	0.01	15	$H_2{}^{18}O$	973.03 ± 0.24	0.81 ± 0.05	0.17 ± 0.019	/
883	0.01	24	$H_2{}^{18}O$	971.41 ± 1.37	0.98 ± 0.15	0.21 ± 0.036	/
853	0.3	2	$H_2{}^{18}O$	977.54 ± 0.43	0.35 ± 0.06	0.08 ± 0.014	/
853	0.3	3	$H_2{}^{18}O$	974.17 ± 0.73	0.70 ± 0.09	0.15 ± 0.022	/
853	0.3	4	$H_2{}^{18}O$	973.87± 1.14	0.73 ± 0.12	/	0.19 ± 0.003

853	0.3	12	$H_2^{18}O$	968.77 ± 1.82	1.25 ± 0.19	0.26 ± 0.050	/
853	0.3	16	$H_2^{18}O$	967.42 ± 1.26	1.39 ± 0.13	/	0.32 ± 0.007
853	0.3	24	$H_2^{18}O$	965.58 ± 2.03	1.57 ± 0.21	/	0.28 ± 0.005
853	0.3	24	$H_2^{16}O$	980.14 ± 1.02	0.09 ± 0.11	/	/
853	0.3	48	$H_2^{16}O$	982.31 ± 1.50	−0.13 ± 0.16	/	/
853	0.3	72	$H_2^{18}O$	962.50 ± 0.65	1.89 ± 0.08	/	0.49 ± 0.01
853	0.3	120	$H_2^{18}O$	960.86 ± 0.48	2.05 ± 0.06	/	/
853	0.3	120	$H_2^{18}O$	961.94 ± 0.99	1.94 ± 0.11	/	0.51 ± 0.005
853	0.3	168	$H_2^{18}O$	961.22 ± 0.72	2.02 ± 0.08	/	0.70 ± 0.006
853	0.3	235	$H_2^{18}O$	crystallized	/	/	/
853	0.01	6	$H_2^{18}O$	975.80 ± 0.34	0.53 ± 0.05	0.11 ± 0.015	/
853	0.01	12	$H_2^{18}O$	973.15 ± 0.62	0.80 ± 0.08	0.17 ± 0.022	/
853	0.01	24	$H_2^{18}O$	970.98 ± 1.52	1.02 ± 0.16	0.22 ± 0.039	/
853	0.01	48	$H_2^{18}O$	966.16 ± 1.62	1.51 ± 0.17	0.32 ± 0.046	/
853	0.01	72	$H_2^{18}O$	962.43 ± 0.99	1.89 ± 0.11	/	/
853	0.01	96	$H_2^{18}O$	963.99 ± 1.28	1.73 ± 0.14	/	/
853	0.01	120	$H_2^{18}O$	961.82 ± 0.68	1.96 ± 0.08	/	/
853	0.01	168	$H_2^{18}O$	961.46 ± 0.91	1.99 ± 0.10	/	/

803	0.3	12	$H_2{}^{18}O$	974.12 ± 1.78	0.70 ± 0.19	0.15 ± 0.042	/
803	0.3	22	$H_2{}^{18}O$	973.27 ± 0.99	0.79 ± 0.11	/	0.18 ± 0.015
803	0.3	48	$H_2{}^{18}O$	969.90 ± 0.91	1.13 ± 0.10	/	0.23 ± 0.002
803	0.3	120	$H_2{}^{18}O$	968.01 ± 1.94	1.33 ± 0.20	0.28 ± 0.050	/
803	0.3	168	$H_2{}^{18}O$	964.96 ± 0.84	1.64 ± 0.09	/	0.37 ± 0.007
803	0.3	336	$H_2{}^{18}O$	962.31 ± 0	1.91 ± 0.04	/	0.44 ± 0.022
803	0.01	36	$H_2{}^{18}O$	973.20 ± 1.16	0.80 ± 0.13	0.17 ± 0.031	/
803	0.01	72	$H_2{}^{18}O$	970.74 ± 0.62	1.05 ± 0.08	0.22 ± 0.026	/
803	0.01	120	$H_2{}^{18}O$	967.03 ± 1.68	1.43 ± 0.18	0.30 ± 0.046	/
803	0.01	168	$H_2{}^{18}O$	965.20 ± 1.41	1.61 ± 0.15	0.34 ± 0.044	/
803	0.01	240	$H_2{}^{18}O$	964.52 ± 1.00	1.68 ± 0.11	/	/
amorphous forsterite (starting material)				981.01 ± 0.04	0	/	0.0019 ± 0.0001
						/	0.0020 ± 0.00009
						/	0.0023 ± 0.0002
						/	0.0018 ± 0.0001
						/	0.0020 ± 0.0001

NOTES.

[a] The peak wavenumber of the 10-µm infrared feature of amorphous forsterite.

[b] Oxygen isotopic compositions ($^{18}O/(^{18}O + ^{16}O)$) of samples obtained from $\Delta\kappa/\kappa_0$.

[c] Oxygen isotopic compositions ($^{18}O/(^{18}O + ^{16}O)$) of samples measured by SIMS.

Table 2.2. Experimental conditions and results for amorphous enstatite annealed with $H_2{}^{16}O$ and $H_2{}^{18}O$ vapor of 0.3 Pa at 803−883 K. Errors represent the 1σ standard deviations of the means.

Temperature (K)	Duration (hour)	Flow gas	Peak position (cm^{-1})[a]	$\Delta\kappa/\kappa_0$ (%)	$f^{18}O$ (SIMS)
923	14	$H_2{}^{18}O$	1027.78 ± 1.29	0.43 ± 0.14	0.15 ± 0.004
923	43	$H_2{}^{18}O$	1024.02 ± 1.99	0.79 ± 0.20	0.24 ± 0.008
923	96	$H_2{}^{18}O$	1021.22 ± 1.61	1.07 ± 0.17	0.32 ± 0.009
923	135	$H_2{}^{18}O$	1020.35 ± 0.81	1.15 ± 0.10	0.38 ± 0.011
923	408	$H_2{}^{18}O$	1013.70 ± 2.14	1.79 ± 0.22	0.57 ± 0.016
953	30	$H_2{}^{16}O$	1030.69 ± 1.57	0.15 ± 0.16	/
953	30	$H_2{}^{18}O$	1024.69 ± 0.73	0.73 ± 0.09	0.24 ± 0.006
953	60	$H_2{}^{16}O$	1030.93 ± 1.62	0.12 ± 0.17	/
953	60	$H_2{}^{18}O$	1021.80 ± 1.69	1.01 ± 0.18	0.33 ± 0.008
953	96	$H_2{}^{18}O$	1019.68 ± 1.84	1.21 ± 0.19	0.41 ± 0.012

953	120	$H_2{}^{18}O$	1018.04 ± 1.89	1.37 ± 0.19	0.44 ± 0.011
953	174	$H_2{}^{18}O$	1015.24 ± 3.04	1.64 ± 0.30	0.51 ± 0.009
953	269	$H_2{}^{18}O$	1012.45 ± 1.18	1.91 ± 0.13	0.61 ± 0.015
978	48	$H_2{}^{18}O$	1021.20 ± 1.20	1.07 ± 0.13	0.37 ± 0.010
978	70	$H_2{}^{18}O$	1019.77 ± 1.46	1.21 ± 0.15	0.45 ± 0.008
978	123	$H_2{}^{18}O$	1015.10 ± 1.90	1.66 ± 0.19	0.57 ± 0.015
978	258	$H_2{}^{18}O$	1012.12 ± 1.55	1.95 ± 0.16	0.72 ± 0.015
1003	20	$H_2{}^{18}O$	1023.92 ± 1.46	0.80 ± 0.15	0.29 ± 0.006
1003	72	$H_2{}^{18}O$	1014.95 ± 0.79	1.67 ± 0.10	0.57 ± 0.014
1003	120	$H_2{}^{18}O$	1009.67 ± 0.82	2.18 ± 0.10	0.71 ± 0.008
1003	121.5	$H_2{}^{18}O$	1011.87 ± 1.58	1.97 ± 0.17	0.70 ± 0.014
1003	148	$H_2{}^{18}O$	1009.36 ± 2.50	2.21 ± 0.25	0.77 ± 0.008
1003	240	$H_2{}^{18}O$	1005.31 ± 0.79	2.61 ± 0.10	0.87 ± 0.011
amorphous enstatite (starting material)	/	/	1032.21 ± 0.64	0	$(2.04 \pm 0.003) \times 10^{-3}$

NOTES.

[a] The peak wavenumber of the 10-μm infrared feature of amorphous enstatite.

Table 2.3. Peak positions of forsterite crystallized at 0.3 Pa of $H_2{}^{16}O$ and $H_2{}^{18}O$ vapor at 953−1123 K.

Temperature (K)	Duration (hr)	Starting material	Gas	Peak positions (cm^{-1})							
953	2	amorphous forsterite	$H_2{}^{18}O$	/	/	910.72[b]	/	610[b]	/	/	/
953	4	amorphous forsterite	$H_2{}^{18}O$	995.5	961.82	903.49	/	605.06[b]	520.20	/	439.69
953	12	amorphous forsterite	$H_2{}^{18}O$	988.34	/	894.81	/	599.75	517.31	461.39	439.21
953	24	amorphous forsterite	$H_2{}^{18}O$	981.11	937.24	889.02	804.17[b]	595.90	513.45	459.94	437.76
953	48	amorphous forsterite	$H_2{}^{18}O$	977.73	935.31	888.54	803.21[b]	595.41	513.94	460.42	437.28
953	92	amorphous forsterite	$H_2{}^{18}O$	976.77	933.86	887.58	798.39	592.52	512.97	456.57	438.24
953	120	amorphous forsterite	$H_2{}^{18}O$	976.29	933.86	887.58	797.90	592.52	509.60	458.49	438.24
953	2	amorphous forsterite	$H_2{}^{16}O$	/	/	914.58[b]	/	610.36[b]	/	/	/
953	12	amorphous forsterite	$H_2{}^{16}O$	1004.25	961.82	911.68/906.38[c]	844.19	615.18	527.92	467.65	441.14
953	120	amorphous forsterite[a]	$H_2{}^{16}O$	1004.73	961.82	908.79/903.01[c]	842.26	616.15	526.95	467.65	441.14
1073	2	amorphous forsterite	$H_2{}^{18}O$	1004.25	960.38	906.86/903.01[c]	842.26	615.66	525.03	465.73	443.07
1073	2	^{18}O-rich amorphous forsterite[a]	$H_2{}^{18}O$	982.55	941.09	885.17	804.65	597.34	510.56	459.46	438.73
1123	72	crystalline forsterite	$H_2{}^{18}O$	1004.73	961.82	908.31/903.49[c]	842.74	616.63	528.4	466.21	442.58

NOTES.

[a] Amorphous forsterite preheated at 853 K and 0.3 Pa of $H_2{}^{18}O$ vapor for 120 hours.

[b] Peak positions determined with naked eyes because of their weak absorbance.

[c] Split peaks.

Analytical procedure

The samples were analyzed with a Fourier transform infrared spectrometer (FT-IR; JASCO FT-IR 4200), X-ray diffractometer (XRD; Rigaku SmartLab), a field emission scanning electron microscope (FE-SEM; JEOL JSM-7000F), and a secondary ion mass spectrometer (SIMS; Cameca ims-6f and -1280HR) at Hokkaido University.

For the FT-IR analysis, a fraction of samples was mixed in KBr powder with a mass ratio of 1:500, and the mixed powder (0.2 g) was pressed into a pellet (10 mm in diameter). Infrared spectra of the samples were obtained with a spectral resolution of 2 cm^{-1} and one hundred scans. The infrared light path was purged with dry nitrogen gas during the analysis. Peak positions in an obtained infrared spectrum were determined using a spectral data analysis software (Spectral manager version2), and several infrared spectra were obtained for the same sample pellet to determine the analytical reproducibility.

For the XRD analysis, the samples were put into a hole (3 mm in diameter and 0.3 mm in depth) on a reflection-free silicon sample holder, and X-ray diffraction patterns were obtained using Cu Kα radiation in the 2θ range from 10° to 70° with a 0.01° step and a scan speed of 1° minute^{-1}.

The samples after oxygen isotope exchange experiments were observed by the FE-SEM in order to study the change of grain shape of amorphous samples due to heating.

Oxygen isotope compositions of the samples were measured with secondary ion mass spectrometry (SIMS). In order to obtain a flat surface for SIMS analysis, the powdery samples were shaped into pellets (3 mm in diameter). The pellet, put in a platinum crucible, was sintered in a vacuum furnace (Tachibana et al. 2011) at 10^{-4}–10^{-5} Pa and ~1100°C for more than 1 day. The vacuum furnace was used to prevent the oxygen isotopic exchange with the surrounding atmosphere during sintering. The sample in the pellet crystallized by sintering, but this does not affect the oxygen isotope analyses. The sintered pellets, mounted into epoxy resin and polished, were measured by SIMS. Oxygen isotopic measurements of sintered forsterite pellets were carried out with Cameca ims-6f. Depth profiles of ^{16}O and ^{18}O were collected from the surface of pellets using a $^{133}Cs^+$ primary beam (10 keV, 3 nA) with a raster area of 70 µm × 70 µm. Negatively charged secondary ions were collected from the central area of the sputtered region (30-µm in diameter). Several depth profiles were obtained for each sample until the ion counts of oxygen isotopes became constant, and the oxygen isotopic compositions of a sample was determined as an average of the compositions from several different depth profiles. A pellet of forsterite crystallized in the vacuum furnace from the starting material without exposure to $H_2{}^{18}O$ vapor was used as a reference in each analytical session. Oxygen isotopic measurements of sintered enstatite pellects were conducted with Cameca ims-1280HR with the measurement procedure reported in Kawasaki et al. (2018). A focused $^{133}Cs^+$ primary beam (20 keV, 0.5 nA) with a diameter of 8 µm was used for the measurements. The primary beam was first rastered over a 20 × 20 μm^2 area for 20–30 seconds for waiting for stabilization of ion intensities (presputtering). The raster size of the primary beam was then reduced to the 10 × 10 μm^2 area, and negative secondary ions ($^{16}O^-$ and $^{18}O^-$) were measured simultaneously in the multi-collection mode using two Faraday cups with 10^{10} Ω resisters for 10–60 seconds. The magnetic field was controlled by a NMR probe. The mass resolution of $M/\Delta M$ was set at ~2000. A normal incident electron flood gun was used for the electrostatic charge compensation of the analyzed area during the measurements. Backgrounds of the Faraday cup detectors were collected by signals without injection of secondary ions during presputtering for each analytical run. Russian spinel ($\delta^{18}O$ = 8.5 ‰ relative to SMOW; Yurimoto et al., 1994) was used as a standard to correct instrumental mass fractionation. Reproducibility of measured $^{18}O/(^{16}O + ^{18}O)$ of the Russian spinel was typically ~0.2 % (1σ standard deviation of the mean). The oxygen isotopic compositions of run products were determined as an average of 10–29 spot analyses.

2.3 *Results*

2.3.1 *Isotopic exchange at 0.3 Pa of water vapor*

Most of the run products with forsterite composition remained amorphous after annealing except for three samples (883 K for 38 and 72 hours and 853 K for 235 hours) heated for longer durations than others (Table 2.1). Typical infrared spectra of samples with forsterite composition heated at 0.3 Pa of $H_2{}^{18}O$ and isotopically-normal water vapor ($H_2{}^{16}O$ hereafter) are compared with the starting material (Fig. 2.2a). The

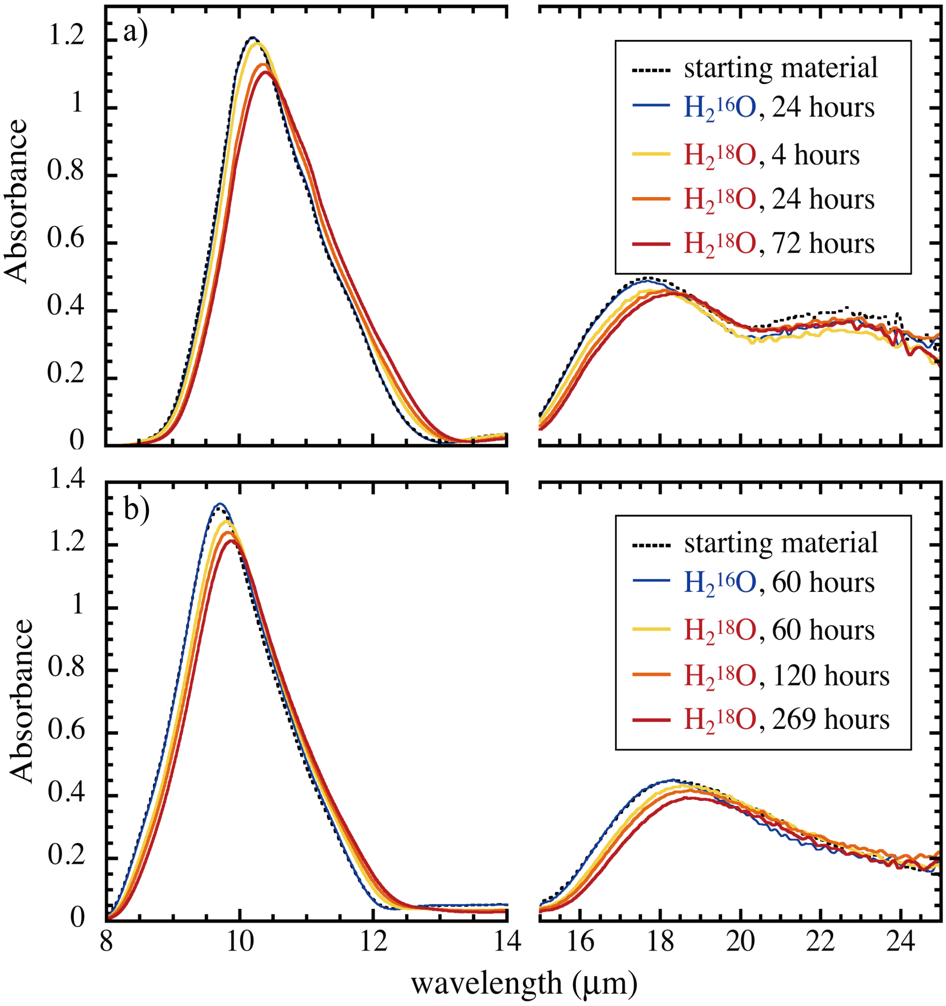

Fig. 2.2. Infrared adsorption spectra of the starting materials (black dotted curves) and the samples with (a) forsterite composition heated at 853 K and 0.3 Pa of $H_2{}^{16}O$ vapor (blue thin solid curve) or $H_2{}^{18}O$ vapor (yellow to red thick solid curves) for different durations and (b) enstatite composition heated at 953 K and 0.3 Pa of $H_2{}^{16}O$ vapor (blue thin solid curve) or $H_2{}^{18}O$ vapor (yellow to red thick solid curves) for different durations.

starting material has a broad peak attributed to Si-O stretching vibration at ~10.2 μm (981 cm^{-1}). The samples heated at 0.3 Pa of $H_2{}^{16}O$ vapor at 853 K for 24 and 48 hours also show the broad feature with the same peak wavelengths (Fig. 2.2a). On the other hand, the peak of amorphous forsterite annealed at 0.3 Pa of $H_2{}^{18}O$ vapor and 803−883 K shifted to a longer wavelength (a lower wavenumber) toward at ~10.4 μm (961 cm^{-1}) with heating duration (Fig. 2.2a; Table 2.1).

Figure 2.2b shows the comparison of typical infrared spectra of run products with enstatite composition heated at 0.3 Pa of $H_2{}^{18}O$ and $H_2{}^{16}O$ vapors with the starting material. No appearance of new peaks for crystalline phases was observed in infrared spectra of all the samples heated at 923–1003 K, showing that the samples remained amorphous during heating. Any change of grains shape was not observed even in samples heated for the longest durations at each temperature. An infrared spectrum of the starting material shows a broad feature of Si-O stretching vibration in the amorphous structure at ~9.69 μm (1032 cm^{-1}). The samples heated at 0.3 Pa of isotopically-normal water vapor showed the broad feature at essentially the same wavelength (Fig. 2.2b and Table 2.2). In contrast, the peak wavelength of the samples heated at 0.3 Pa of $H_2{}^{18}O$ vapor gradually shifted to longer wavelength with time (Fig. 2.2b and Table 2.2).

Similar peak wavelength shifts were observed for the 18-μm absorption featuress of amorphous forsterite and enstatite, representing the Si-O-Si bending vibration, for the samples heated with $H_2{}^{18}O$ vapor (Figs. 2.2a and 2.2b).

Figure 2.3 shows the relative peak shifts of the 10-μm feature ($\Delta\kappa/\kappa_0$) of amorphous forsterite and enstatite, where κ_0 is the peak wavenumber of the starting material and $\Delta\kappa$ represents a difference in peak wavenumbers of the sample and the starting material ($\kappa_0 - \kappa_{sample}$). Although the $\Delta\kappa/\kappa_0$ remains constant within analytical error for samples heated with $H_2{}^{16}O$ vapor of 0.3 Pa, it increases with time for the samples heated with $H_2{}^{18}O$ vapor for each temperature. In the case of amorphous forsterite, the $\Delta\kappa/\kappa_0$ becomes almost constant for further heating after it reaches ~2%

(Fig. 2.3).

Linear correlations between $\Delta\kappa/\kappa_0$ for the 10-μm infrared feature and the oxygen isotopic compositions were observed up to $^{18}O/(^{16}O + ^{18}O)$ (= $f^{18}O$) of 0.4, where

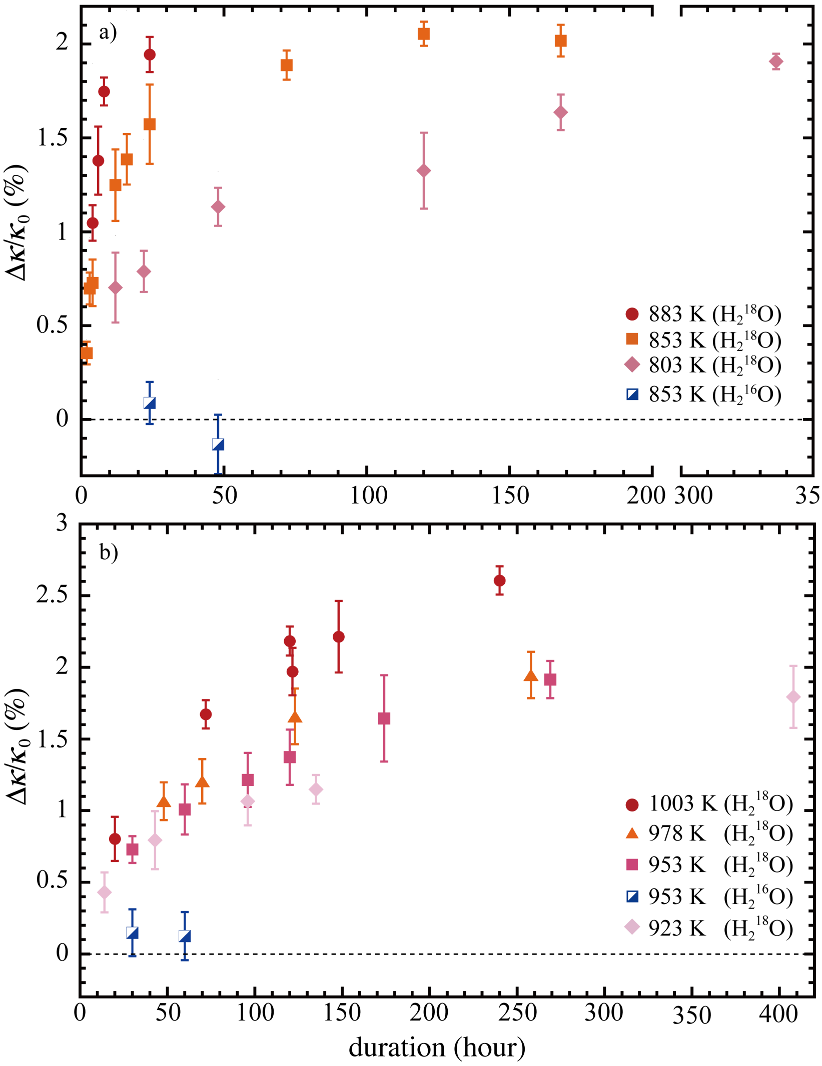

Fig. 2.3. Relative peak shifts ($\Delta\kappa/\kappa_0$; see text in detail) of the 10-μm infrared absorption feature of the samples with (a) forsterite composition heated at 0.3 Pa of $H_2{}^{18}O$ vapor at 803, 853, and 883 K for different durations and (b) enstatite composition heated at 0.3 Pa of $H_2{}^{18}O$ vapor at 923, 953, 978, and 1003 K for different durations. The $\Delta\kappa/\kappa_0$ of the samples heated at 0.3 Pa of $H_2{}^{16}O$ vapor and 853 K for amorphous forsterite and at 953 K for amorphous enstatite are also shown for comparison. Error bars represent the 1σ standard deviations of the means of several measurements of the same sample.

$\Delta\kappa/\kappa_0$ reaches to the constant value of ~2%, for amorphous forsterite and in all the range of $f^{18}O$ for amorphous enstatite (Fig. 2.4; Tables 2.1 and 2.2). These correlations suggests that $\Delta\kappa/\kappa_0$ for 10-μm infrared features can be used as a scale of oxygen isotopic compositions with $f^{18}O < \sim 0.4$ for amorphous forsterite and $f^{18}O < \sim 1$ for amorphous enstatite.

Typical infrared spectra of the samples with forsterite composition annealed at 953 K and 0.3 Pa of $H_2{}^{18}O$ and $H_2{}^{16}O$ vapor are compared in Fig. 2.5 (See also Table 2.3 for peak positions of all the samples). The amorphous forsterite gradually crystallizes with time at this temperature, which is also confirmed with X-ray diffraction. Although the spectra of forsterite crystallized in the presence of $H_2{}^{18}O$ vapor resemble overall to that of the isotopically-normal crystalline forsterite, all the peaks shifted to longer wavelengths (lower wavenumbers) as crystallization proceeded (Fig. 2.5).

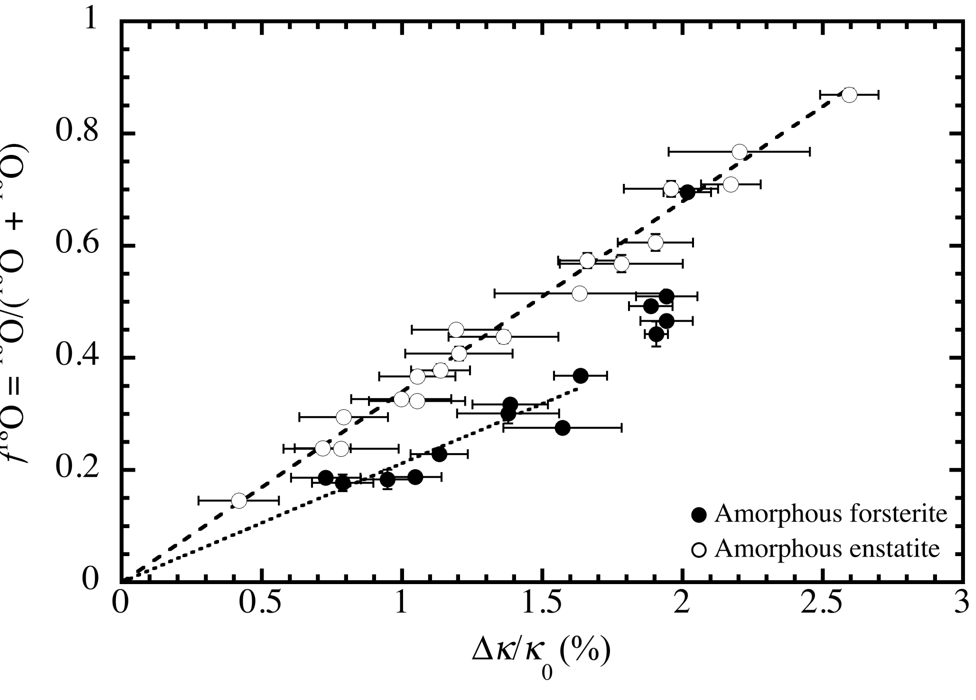

Fig. 2.4. Comparison of oxygen isotopic composition $f^{18}O = {}^{18}O/({}^{18}O + {}^{16}O)$ and $\Delta\kappa/\kappa_0$ for amorphous forsterite (filled symbols) and amorphous enstatite (open symbols). A linear correlation between $f^{18}O$ and $\Delta\kappa/\kappa_0$ of <~1.64% for amorphous forsterite is shown as a dotted line, and that between $f^{18}O$ and $\Delta\kappa/\kappa_0$ for amorphous enstatite is shown as a dashed line. Error bars are the 1σ standard deviations of the means.

Another notable feature is that the peaks were broader than those of the isotopically-normal crystalline forsterite.

An infrared spectrum of the sample with forsterite composition heated at 1073 K and 0.3 Pa of $H_2{}^{18}O$ vapor for 2 hours matches the crystalline forsterite having the normal oxygen isotopic composition, and neither peak shift nor significant peak broadening was observed (Fig. 2.6; Table 2.3). I also conducted a heating experiment at the same condition using the amorphous forsterite that was once annealed at 853 K and 0.3 Pa of $H_2{}^{18}O$ vapor for 120 hours as a starting material. The run product also shows the infrared feature of crystalline forsterite, but all the peaks shifted to longer wavelengths without significant peak broadening (Fig. 2.6; Table 2.3).

An oxygen isotopic exchange experiment between crystalline forsterite submicron-sized grains and water vapor was also conducted at a higher temperature of 1123 K and 0.3 Pa of $H_2{}^{18}O$ vapor for 72 hours. Neither peak shift nor peak broadening was observed (See also Table 2.3).

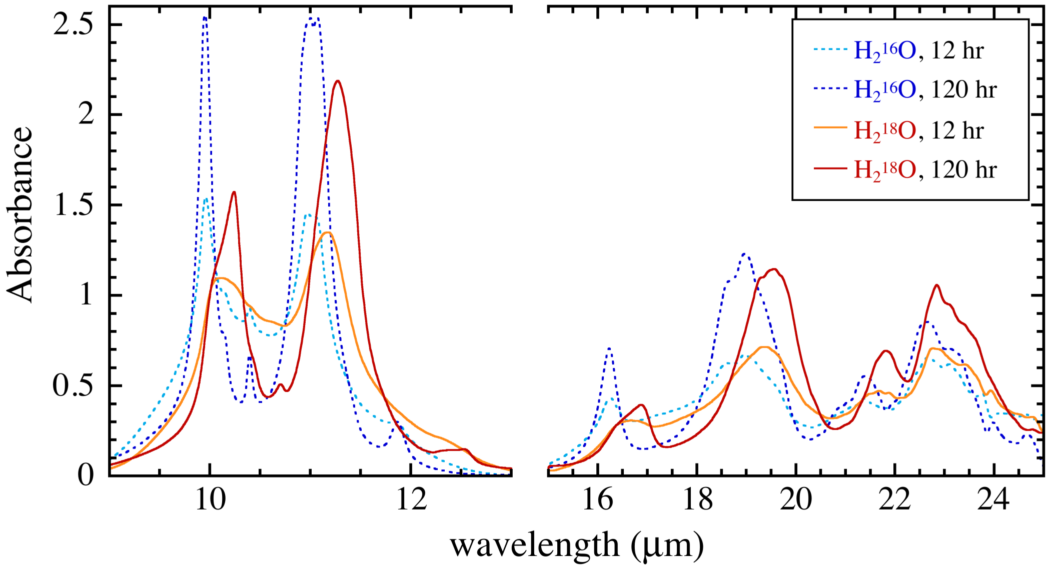

Fig. 2.5. Infrared adsorption spectra of samples with forsterite composition heated at 0.3 Pa of $H_2{}^{16}O$ or $H_2{}^{18}O$ vapor for 12 and 120 hours at 953 K.

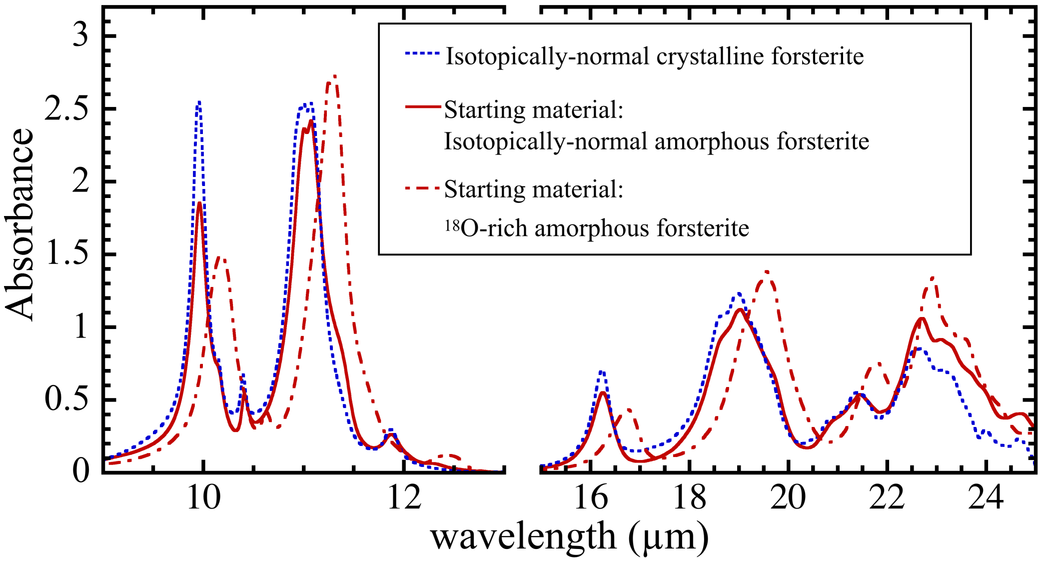

Fig. 2.6. An infrared spectrum of forsterite crystallized at 1073 K and 0.3 Pa of $H_2{}^{18}O$ vapor for 2 hours from the starting material with forsterite composition (red solid curve). The spectrum of forsterite crystallized at the same condition from amorphous forsterite that was preheated at 853 K and 0.3 Pa of $H_2{}^{18}O$ vapor for 120 hours is shown as a red dot-dashed curve. An infrared spectrum of the isotopically-normal crystalline forsterite is also shown for comparison (blue dotted curve).

2.3.2 *Isotopic exchange at 0.01 Pa of water vapor*

Oxygen isotopic exchange experiments between amorphous forsterite and water vapor were also conducted at 0.01 Pa of $H_2{}^{18}O$ vapor. The samples heated at 883, 853, and 803 K and 0.01 Pa of $H_2{}^{18}O$ vapor did not crystallize and remained amorphous forsterite. The 10- and 18-μm infrared absorption features shifted to longer wavelengths (shorter wavenumbers) with time as observed in the samples heated at 0.3 Pa of $H_2{}^{18}O$ vapor (Fig. 2.7a; See also Table 2.1). The time evolution of $\Delta\kappa/\kappa_0$ of the 10-μm infrared features of the samples heated at 883 and 853 K are similar to each other, suggesting that the oxygen isotopic exchange rates at these temperatures are almost the same.

The time evolution of $\Delta\kappa/\kappa_0$ of the samples heated at 0.01 Pa and 0.3 Pa of $H_2{}^{18}O$ vapor are compared in Fig. 2.7b–d. At 883 K, $\Delta\kappa/\kappa_0$ at 0.01 Pa of $H_2{}^{18}O$ vapor evolves more slowly than that at 0.3 Pa (Fig. 2.7b), suggesting that the isotopic exchange rate at 0.01 Pa is smaller than that at 0.3 Pa. The difference between the temporal changes of $\Delta\kappa/\kappa_0$ at 0.01 and 0.3 Pa becomes smaller with decreasing temperature. The isotopic exchange at 0.01 Pa seems to have proceeded with a bit smaller rate than that at 0.3 Pa and 853 K (Fig. 2.7c), and it proceeded at a similar rate at 0.01 and 0.3 Pa (Fig. 2.7d).

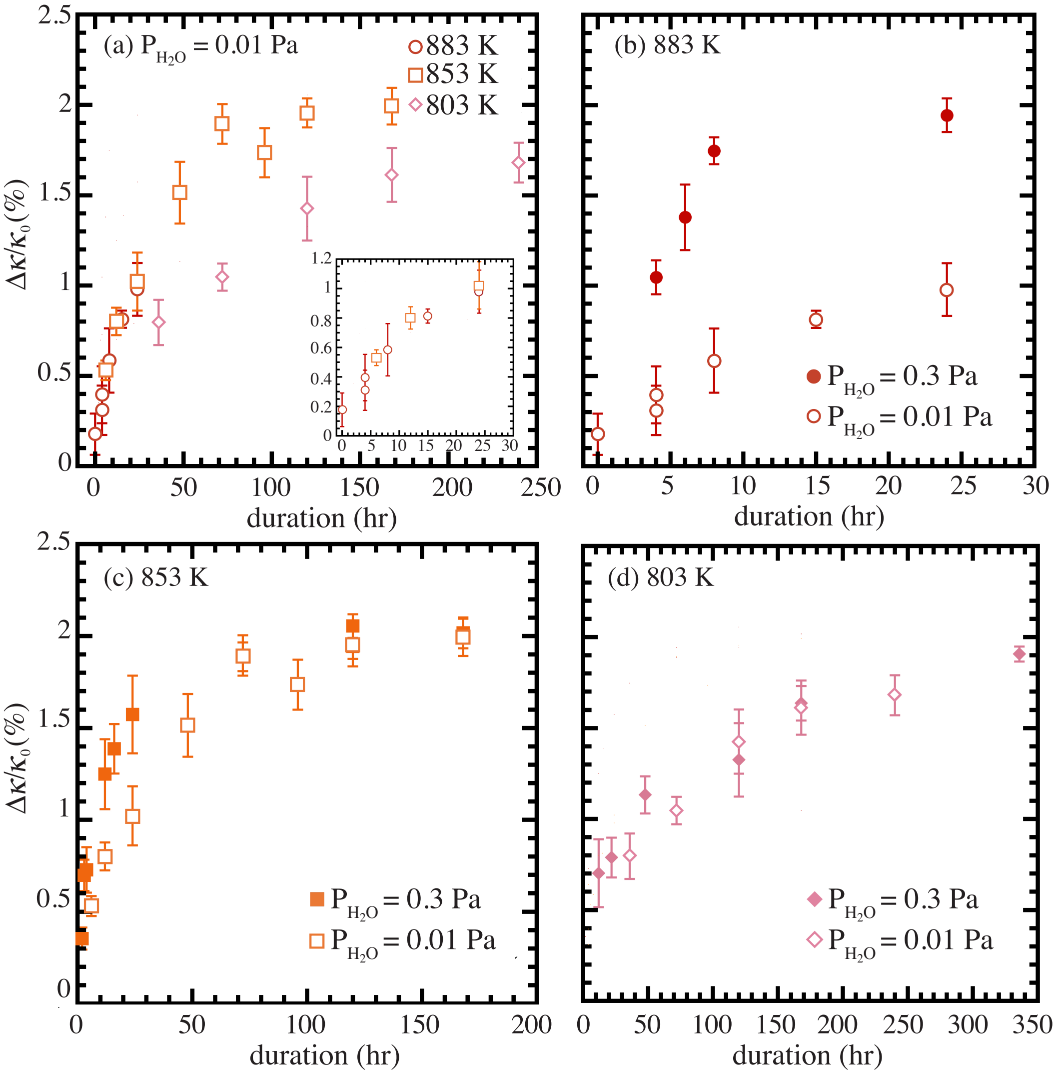

Fig. 2.7. (a) Temporal changes of relative peak shifts ($\Delta\kappa/\kappa_0$) of the 10-μm infrared absorption feature of amorphous forsterite heated at 803, 853, and 883 K and 0.01 Pa of $H_2{}^{18}O$. An inset shows the temporal change of $\Delta\kappa/\kappa_0$ for shorter heating durations. Error bars represent the 1σ standard deviations of the means of several measurements of the same sample. (b) Temporal changes of $\Delta\kappa/\kappa_0$ at 0.01 and 0.3 Pa of $H_2{}^{18}O$ vapor at 883 K, (c) 853 K, (d) 803 K.

2.4 *Discussion*

2.4.1 *Isotopic exchange reaction kinetics at 0.3 Pa of water vapor*

The oxygen isotopic compositions ($f^{18}O$) of the samples heated at 803, 853, and 883 K for amorphous forsterite and at 923, 973, 978, and 1003 K for amorphous enstatite, measured with SIMS, are normalized to the isotopic composition of $H_2{}^{18}O$ ($f^{18}O = 0.97$) to express the degrees of the isotopic exchange of the sample (α). I also estimated α of the samples that were not measured by SIMS based on the linear correlation of amorphous forsterite between $\Delta\kappa/\kappa_0$ and $f^{18}O$ (Fig. 2.4) when their $\Delta\kappa/\kappa_0$ were smaller than 1.64%.

Temporal changes of α for amorphous forsterite and enstatite at each temperature are shown in Fig. 2.8. A possible rate-limiting step for oxygen isotope exchange between amorphous silicate grains and water vapor at low P_{H2O} is either a supply of water molecules from vapor or a diffusive isotope exchange process inside amorphous. In the case of water supply-controlled isotopic exchange reaction, the supply flux of water molecules (J_w) depends on P_{H2O} and the mean velocity of water molecules;

$$J_w = \frac{P_{\mathrm{H_2O}}}{\sqrt{2\pi mkT}}\,, \tag{2.1}$$

where m is a molecular weight of H_2O, k is the Boltzmann constant, and T is the absolute temperature. The oxygen isotopic exchange rate can be expressed as;

$$\frac{d\alpha}{dt} = \frac{\beta J_w S(1-\alpha)}{\gamma(V/\Omega)N_A}\,. \tag{2.2}$$

where β is a dimensionless parameter to express the isotope exchange efficiency of colliding water molecules at the grain surface ($0 < \beta \leq 1$), S is the grain surface area, γ is the atomic ratio of oxygen in the gas and solid phases (4 for amorphous forsterite and 3 for amorphous enstatite), V is a grain volume, Ω is a molar volume of amorphous silicate, N_A is Avogadro's number, and t is time. The term of $1-\alpha$ was included because the isotope exchange rate decreases with increasing α due to the decrease of ^{16}O in the samples. The integral expression of Eq. (2.2) is given by,

$$\alpha = 1 - \exp\left(-\frac{\beta J_w S}{\gamma\left(V/\Omega\right)N_A} t \right).$$ (2.3)

If the oxygen isotope exchange reaction is controlled by the diffusive isotope exchange in the amorphous structure, the temporal change of α should follow the three-dimensional diffusion equation in a sphere expressed as follows (Crank, 1975);

$$\alpha = 1 - \sum_{n=1}^{\infty} \frac{6}{n^2\pi^2} \exp\left(-\frac{Dn^2\pi^2 t}{r^2} \right),$$ (2.4)

where D is the diffusive isotope exchange rate constant and r is a grain radius (40 nm on average for amorphous forsterite and 35 nm for amorphous enstatite).

The temporal change of α for amorphous forsterite and enstatite is better explained by the three-dimensional spherical diffusion equation (Eq. (2.4)) than the water supply-controlled reaction equation (Eq. (2.3)) at all the experimental temperatures (Fig 2.8), suggesting that oxygen isotope exchange reactions at 803–883 K for amorphous forsterite and 923–1003 K for amorphous enstatite and $P_{\mathrm{H2O}} = 0.3$ Pa are governed by diffusive isotope exchange reaction in the amorphous structure. The obtained diffusive isotope exchange rate constants for amorphous forsterite at 803, 853, and 883 K are $(4.9 \pm 0.6) \times 10^{-23}$, $(1.9 \pm 0.8) \times 10^{-22}$, and $(4.4 \pm 0.8) \times 10^{-22}$ m^2 s^{-1}, respectively, and those for amorphous enstatite at 923, 953, 978, and 1003 K are $(4.3 \pm 0.06) \times 10^{-23}$, $(6.9 \pm 0.1) \times 10^{-23}$, $(1.2 \pm 0.02) \times 10^{-22}$, and $(2.2 \pm 0.03) \times 10^{-22}$ m^2 s^{-1}, respectively. The D shows the Arrhenius relation (Fig. 2.9), yielding D [m^2 s^{-1}] = $(1.5 \pm 1.0) \times 10^{-19} \exp[-(161.5 \pm 14.1\ (\mathrm{kJ\ mol^{-1}}))\ R^{-1}\ (1/T-1/1200)$ for amorphous forsterite and D (m^2 s^{-1}) = $(5.0 \pm 0.2) \times 10^{-21} \exp[-(161.3 \pm 1.7\ (\mathrm{kJ\ mol^{-1}}))\ R^{-1}\ (1/T-1/1200)]$ for amorphous enstatite. The term of −1/1200 was included to reduce the uncertainty of the pre-exponential term. This expression of D is valid only below 1200 K, but the extrapolation to >1200 K is meaningless because crystallization of amorphous forsterite and enstatite proceeds with a minute or less (Murata et al., 2009; Yamamoto and Tachibana, 2018) at a much faster rate than the oxygen isotopic exchange at 1200 K as discussed below. The activation energy of *D* for amorphous enstatite (~161 kJ mol^{-1}) is essentially the same as that for amorphous forsterite (~162 kJ mol^{-1}). This suggests that the overall energetic barrier for the exchange reaction, which should include those of diffusion and oxygen replacement, is the same for amorphous enstatite and forsterite. However, the *D* for amorphous enstatite is ~30 times smaller than that for amorphous forsterite due to the smaller pre-exponential term. This may reflect factors related to the pre-exponential term such as reaction frequency, numbers and kinds of diffusion pathways, and a fraction of non-bridging oxygen (e.g. Kalampounias et al., 2009; Kuroda et al., 2018).

Crystallization of amorphous forsterite occurred at 1073 K, and the infrared spectrum is the same as that of isotopically-normal crystalline forsterite and shows neither peak shift and nor significant peak broadening (Fig. 2.6). The crystallization experiments at 1073 K for the amorphous forsterite pre-heated at 853 K and 0.3 Pa of $H_2{}^{18}O$ vapor for 120 hours found that the run product shows the infrared spectrum of crystalline forsterite with shifts of all the peak positions to longer wavelengths (Fig. 2.6). Because the amorphous forsterite exposed to $H_2{}^{18}O$ (0.3 Pa) at 853 K for 120 hours should be enriched in ^{18}O as discussed above, the observed shifted peaks represent the infrared feature of ^{18}O-rich crystalline forsterite. These observations suggest that crystallization occurs faster than oxygen isotopic exchange at 1073 K and that crystalline forsterite does not exchange oxygen isotopes with water vapor as efficiently as amorphous forsterite does. The experiments with crystalline forsterite at 1123 K and 0.3 Pa of $H_2{}^{18}O$ vapor has also shown that crystallization of amorphous forsterite occurs fast and the oxygen isotopic exchange between with crystalline forsterite and water vapor is not as fast as that for amorphous forsterite. This is because crystalline forsterite is nominally anhydrous mineral and does not contain water molecules inside its structure as much as amorphous forsterite does. The slower oxygen isotopic exchange rate with crystalline forsterite is also supported by oxygen self-diffusion rate in crystalline forsterite (Jaoul et al., 1980).

Crystallization of amorphous forsterite occurred for the samples heated at 953 K and 0.3 Pa of $H_2{}^{18}O$ vapor, and all the peaks of crystalline forsterite shifted to longer wavelengths with time and became broader than those of isotopically-normal crystalline forsterite with crystallization (Fig. 2.5). This can be interpreted as that crystallization of amorphous forsterite proceeds after incomplete oxygen isotopic exchange of amorphous forsterite at this temperature. Crystalline forsterite can keep the oxygen isotopic composition at the timing of their crystallization because of the sluggish isotopic exchange reaction as observed at higher temperatures of 1073 and 1123 K. Thus forsterite crystallizing in the early stage can be ^{16}O-rich, while that crystallizing in the late stage can be enriched in ^{18}O because the isotopic exchange between the amorphous forsterite and $H_2{}^{18}O$ proceeds with time. In this case, the infrared spectrum of run products should be a mixture of those of crystalline forsterite with a wide range of oxygen isotopic compositions, resulting in the spectrum with broader peaks shifted to longer wavelengths.

It has been known that the change of grain shape and size through sintering during annealing also affects the peak positions and peak widths (e.g. Koike et al. 2010). However, Koike et al. (2010) found that, unlike to other peaks of crystalline forsterite, the peak at 11.9 μm is insensitive to the change of grain shape. In the present experiments, we observed that the 11.9-μm peak also shifted to a longer wavelength (Fig. 2.5). In fact, no grain shape change of the annealed sample heated at 953 K and 0.3 Pa of $H_2{}^{18}O$ vapor for 24 hours was observed by SEM. Therefore, we conclude that the peak shifts and peak broadening at 953 K were not caused by the changes of grain shape and size, but by simultaneous crystallization and oxygen isotopic exchange of amorphous forsterite.

The activation energies of these competing reactions are ~162 kJ mol^{-1} for the diffusive exchange rate constant (Fig. 2.9) and ~357 kJ mol^{-1} for crystallization at P_{H2O} of 0.3 Pa (Yamamoto and Tachibana, 2018), respectively. Hence, crystallization proceeds at a larger rate at higher temperatures such as 1073 K, while the isotopic exchange of amorphous forsterite occurs faster at lower temperatures such as <883 K. The transition temperature for the two competing processes would be close to 953 K.

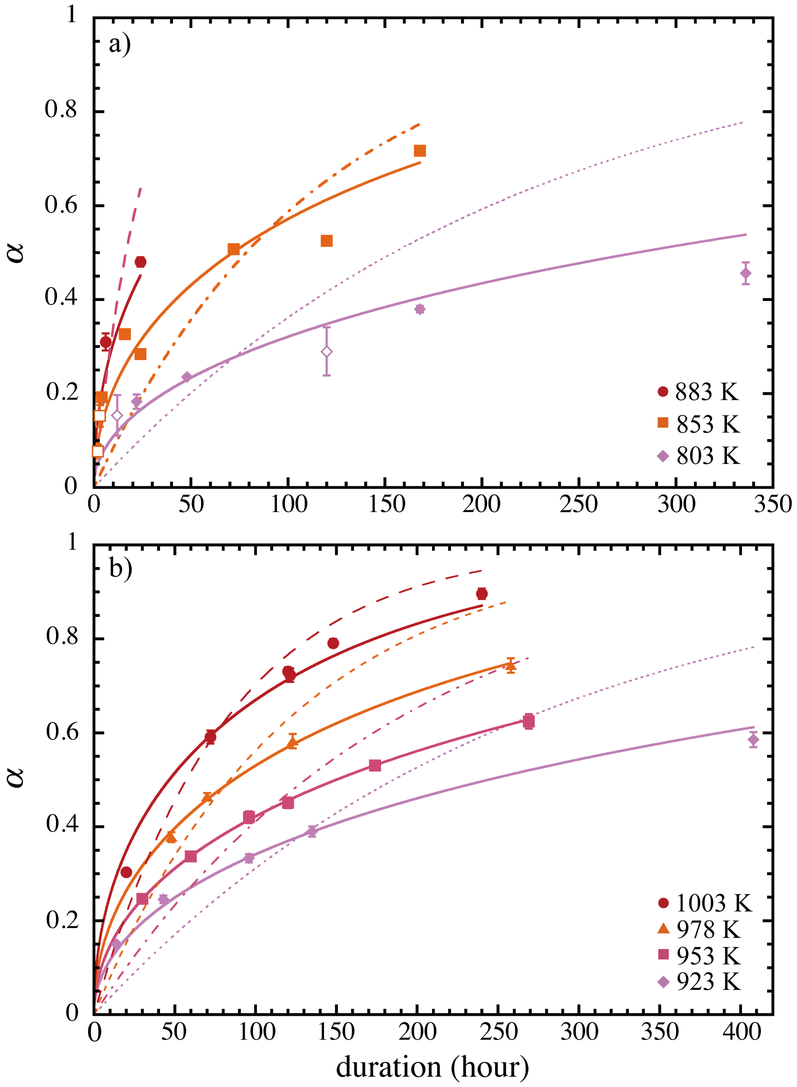

Fig. 2.8. Time evolution of the degree of oxygen isotopic exchange (α) of (a) amorphous forsterite heated at 0.3 Pa of $H_2{}^{18}O$ vapor and 803, 853, and 883 K and of (b) amorphous enstatite heated at 0.3 Pa of $H_2{}^{18}O$ vapor and 923, 953, 978, and 1003 K. Closed symbols are the data measured by SIMS, and open symbols are those estimated from $\Delta\kappa/\kappa_0$ (%) of samples. The solid curves represent the best-fitted curves of the three-dimensional spherical diffusion equation (Eq. (2.4)). The dotted, dotted-dashed, and long dashed curves in (a) represent the best-fitted curves of water supply-controlled reaction (Eq. (2.3)) at 803, 853, and 883 K, respectively, and the dotted, dotted-dashed, short dashed, and long dashed curves in (b) represent the best-fitted curves of water supply-controlled reaction (Eq. (2.3)) at 923, 953, 978, and 1003 K, respectively. Errors bars are the 1σ standard deviations of the means.

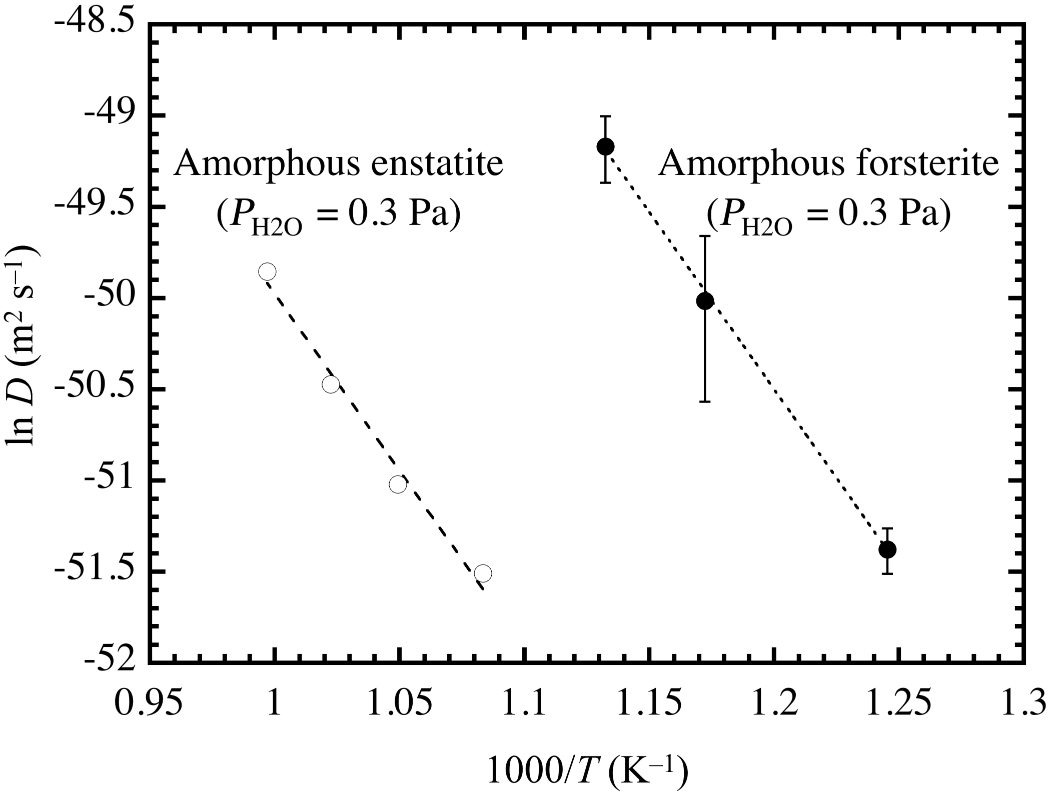

Fig. 2.9. Temperature dependence of the diffusive isotopic exchange rate constant (*D*) for amorphous forsterite (filled symbols) and enstatite (open symbols) at P_{H2O} of 0.3 Pa. Arrhenius linear regressions for amorphous forsterite and enstatite are shown as dotted and dashed lines, respectively. Error bars represent the 1σ standard deviations of the means.

2.4.2 *Isotopic exchange reaction kinetics at 0.01 Pa of water vapor*

Temporal changes of oxygen isotopic compositions of the samples with forsterite composition heated at 0.01 Pa of $H_2{}^{18}O$ vapor at 803, 853, and 883 K are summarized in Fig. 2.7. Oxygen isotopic exchange proceeded at smaller reaction rates at 0.01 Pa of $H_2{}^{18}O$ vapor and 883 and 853 K than those at 0.3 Pa of $H_2{}^{18}O$ vapor (Figs. 2.7b and 2.7c). Moreover, the data suggest that the reaction proceeded at almost the same rate at 883 and 853 K at 0.01 Pa of water vapor (Fig. 2.7a). These cannot be explained by the diffusive isotopic exchange reaction that controls the overall reaction rate at 0.3 Pa of water vapor, and should be controlled by a different process.

Another plausible rate-limiting process would be a supply of water molecules as discussed above, and the J_w in Eq. (2.1) does not largely depend on temperature, and could explain a very weak temperature dependence of the reaction rate at 883 and 853 K. Moreover, the J_w at 0.01 Pa should be 30 times smaller than that at 0.3 Pa. The supply of water molecules could thus become a rate-limiting process under the lower P_{H2O} conditions. When the exchange fraction is small, the temporal change of α in Eq. (2.2) can be expressed approximately as;

$$\frac{d\alpha}{dt} = \frac{\beta J_w S}{\gamma\left(V/\Omega\right)n_A}, \qquad (2.5)$$

Equation (2.5) shows that α changes linearly with time when the supply of water molecules is the rate-limiting process.

The degrees of isotopic exchange (α) of amorphous forsterite heated at 883 and 853 K with 0.01 Pa of $H_2{}^{18}O$ vapor (Fig. 2.10; Table 2.1) show a linear relation with time. Because the sample that was heated for 0 minutes at 883 K showed a small degree of isotopic exchange ($\alpha \sim 0.03$) due to the isotopic exchange upon heating to 883 K, we focus on the slope of the data in Fig. 2.10. The linear regression gives β of $(7.4 \pm 1.2) \times 10^{-6}$ for the average grain radius of 40 nm.

At 803 K, isotopic exchange proceeded at the identical rate both at 0.01 and 0.3 Pa of $H_2{}^{18}O$ vapor, and the rate at 0.01 Pa of $H_2{}^{18}O$ vapor was slower than those controlled by the supply of water molecules at 883 and 853 K (Fig. 2.7d). This suggests that the supply of water molecules is not the rate-limiting step at 803 K and 0.01 Pa of water vapor. The identical reaction rate at 0.01 and 0.3 Pa of $H_2{}^{18}O$ vapor can be explained by the diffusion-controlled isotopic exchange that is expected to have little or no dependence on P_{H2O}.

I thus conclude that the oxygen isotopic exchange rate between amorphous forsterite and water vapor is controlled by the supply of water molecules at lower P_{H2O} and higher temperatures, while it is controlled by the diffusive isotopic exchange reaction within the amorphous structure at higher P_{H2O} and lower temperatures. In the present experimental conditions, the transition of the rate limiting step occurs at ~850 K and P_{H2O} of 0.01 Pa.

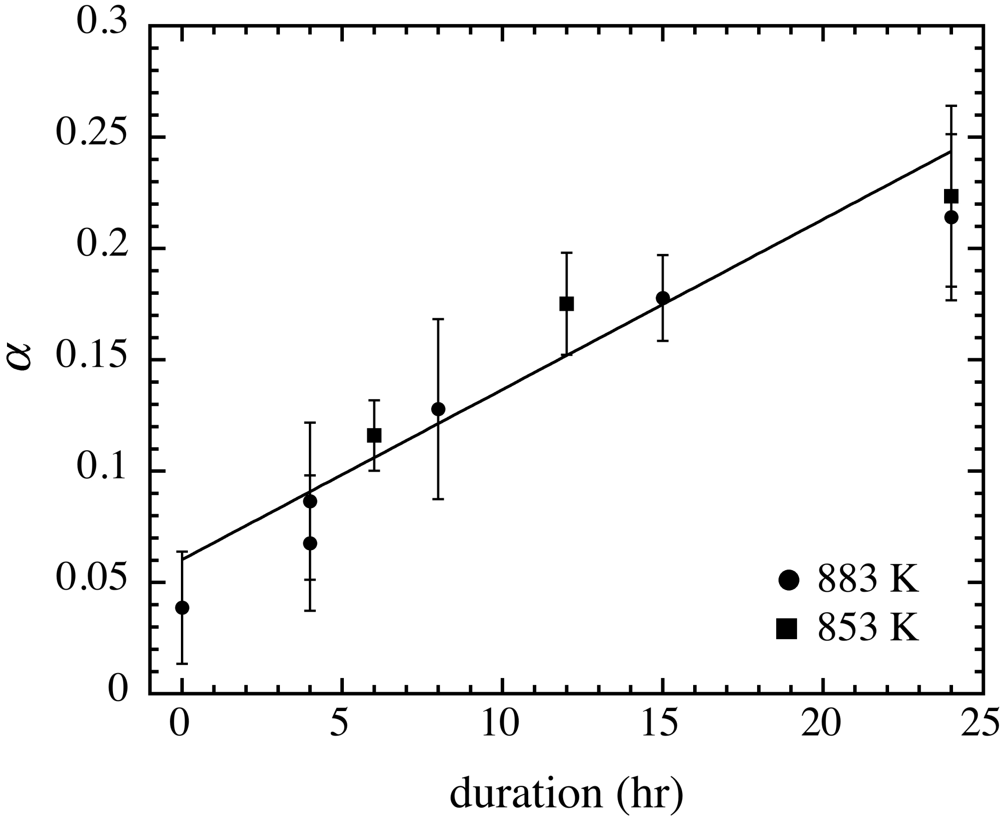

Fig 2.10. Time evolution of the degree of oxygen isotopic exchange (α) of amorphous forsterite obtained from $\Delta\kappa/\kappa_0$ of samples heated at 883 K (circle) and 853 K (square) and 0.01 Pa of $H_2{}^{18}O$ vapor. Solid line represents the best-fitted line by Eq. (2.5). Error bars are the 1σ standard deviations of the means.

2.5 *Application to oxygen isotopic exchange of amorphous silicates in the protoplanetary disks*

I evaluated the timescale of oxygen isotopic exchange of amorphous forsterite and enstatite grains and those of other related reactions in protoplanetary disks. Grain diameters of 0.1 and 1 μm were chosen for calculation because matrix silicate grains in chondrites are typically up to ~1 μm in size (Pontoppidan and Brearley 2010 and references therein).

Amorphous forsterite

The blue solid curves in Fig. 2.11 show the timescales of diffusive isotopic exchange given as r^2/D that corresponds to the time required for $\alpha \sim 1$. The timescales of diffusive oxygen isotopic exchange of amorphous forsterite dust are shorter than the typical lifetime of gas in protoplanetary disks (1−10 Myr; Pascucci and Tachibana 2010 and references therein) at temperatures above 500–600 K for 0.1-μm- and 1-μm-sized grains.

The supply of water molecules from the disk gas can govern the reaction at higher temperatures and lower P_{H2O}. The timescales of oxygen isotopic exchange controlled by the supply of water molecules for $\alpha = 0.99$ calculated using Eq. (2.3) with β of 7.4×10^{-6} are also shown in Fig. 2.11 for 0.1-μm- and 1-μm-sized amorphous forsterite dust at different P_{H2O} (10^{-1} and 10^{-4} Pa) (dotted curves). P_{H2O} of 10^{-1} and 10^{-4} Pa are chosen as possible upper and lower limits in the protosolar disk assuming the total pressures ranging from 10^2 and 10^{-1} Pa with $H_2/H_2O \sim 10^3$ (Wood and Morfill, 1988; Lodders, 2003). The timescale has a linear dependence on P_{H2O} (Eqs. (2.1) and (2.2)), and it takes three orders of magnitude longer time for isotopic exchange at 10^{-4} Pa than that at 10^{-1} Pa. Within the possible range of P_{H2O} in protoplanetary disks, the oxygen isotopic exchange timescale of amorphous forsterite would be controlled by the supply of water molecules at > ~750 K for P_{H2O} of 10^{-4} Pa and at > ~1000 K for P_{H2O} of 10^{-1} Pa, if the grains remain amorphous, because the gas flux does not have a large temperature dependence (Eq. (2.1)). I note that β may depend on temperature and might be larger at higher temperatures. If this were the case, the reaction timescale would become shorter at higher temperatures.

Crystallization of amorphous forsterite due to thermal annealing is also considered. The timescale of crystallization of 0.08-μm-sized amorphous forsterite grains (Yamamoto and Tachibana, 2018) at P_{H2O} of 10^{-1} and 10^{-4} Pa are also shown in Fig. 2.11 (short dashed and dot-dashed curves, respectively). The grain size would not affect significantly the crystallization timescale according to the kinetics reported in Yamamoto and Tachibana (2018), where crystallization occurs from pre-existing nuclei in the grains. Because the activation energy for crystallization of amorphous forsterite

(254−414 kJ mol^{-1} for P_{H2O} of 10^{-4}−500 Pa) is larger than that for the diffusive isotopic exchange reaction, amorphous forsterite can crystallize prior to the oxygen isotopic exchange if the grains are rapidly heated at temperatures above 800−900 K as observed in this study.

The oxygen isotopic exchange between crystalline forsterite and water vapor would be controlled by the supply of water molecules or self-diffusion of oxygen within the crystalline structure. The timescales of oxygen self-diffusion in 0.1-μm- and 1-μm-sized crystalline forsterite grains (Jaoul et al. 1980) are also shown in Fig. 2.11 (long dashed curves). The β for the water supply-controlled isotopic exchange for crystalline forsterite is not known, but may not be significantly smaller than that for amorphous forsterite. If the same β can be used, the timescales of isotopic exchange for crystalline forsterite controlled by the supply of water molecules are the same as those for amorphous forsterite (dotted curves in Fig. 2.11), and the oxygen isotopic exchange should occur by oxygen self-diffusion within crystalline forsterite. The diffusive isotopic exchange between crystalline forsterite and water vapor is significantly slower than that for amorphous forsterite. The timescale for isotopic exchange of crystalline forsterite would be ~4−5 orders of magnitude longer than that for amorphous forsterite (Fig. 2.11), and the effective isotopic exchange would not occur with short-duration heating at ~1000 K. In this case, the original isotopic signature of amorphous forsterite dust would be kept in crystalline forsterite dust transformed from the amorphous forsterite. I note that the effect of crystallographic orientation on the diffusivity of oxygen in crystalline forsterite would not be more noticeable than temperature as in the case of oxygen self-diffusion in crystalline olivine (Ryerson et al., 1989), and crystallographic orientation does not affect the diffusive isotopic exchange timescale for crystalline forsterite significantly.

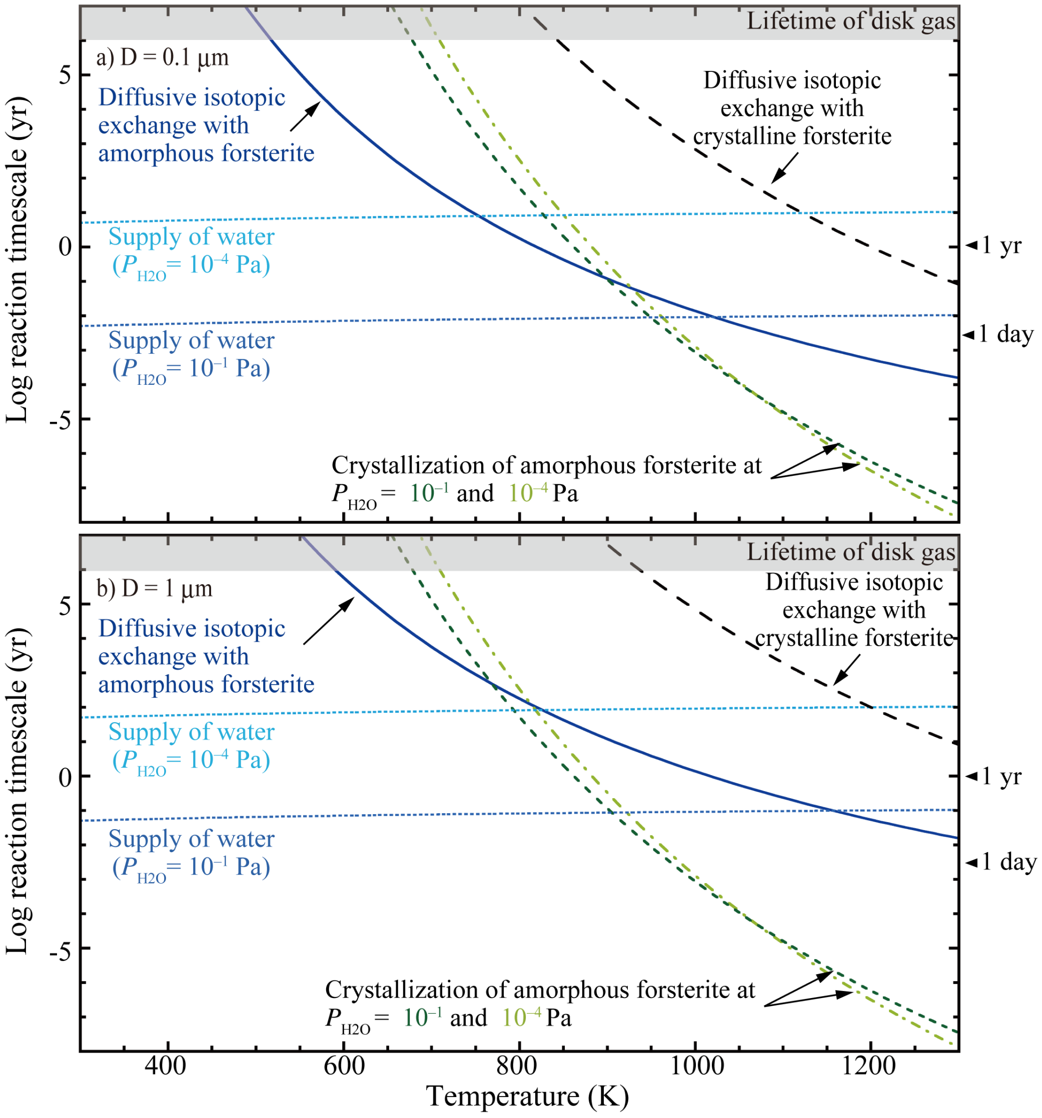

Fig. 2.11. Timescales of oxygen isotopic exchange between amorphous forsterite dust and water vapor in protoplanetary disks controlled by the diffusive isotopic exchange reaction (blue solid curves) and by the supply of water molecules at P_{H2O} of 10^{-1} and 10^{-4} Pa (blue dotted curves). Timescales of oxygen self-diffusion in crystalline forsterite (black long dashed curves; Jaoul et al., 1980) and of crystallization of amorphous forsterite at P_{H2O} of 10^{-1} and 10^{-4} Pa (green short dashed and dot-dashed curves, respectively; Yamamoto & Tachibana, 2018) are shown for comparison. The estimated lifetime of protoplanetary disk gas (1–10 Myr) is also shown for comparison. (a) 0.1 µm. (b) 1 µm.

Amorphous enstatite

The blue solid curves in Fig. 2.12 show the timescale of diffusive isotopic exchange of amorphous enstatite for $\alpha \sim 1$. Because the activation energies for the reaction of amorphous enstatite and forsterite are identical to one another (Fig. 2.9), the isotope exchange timescale for amorphous enstatite is ~30 times longer than that for amorphous forsterite in a wide range of temperature when the diffusive isotope exchange reaction is a rate-limiting step for amorphous enstatite and forsterite (Figs. 2.11 and 2.12). The timescales of diffusive oxygen isotope exchange of amorphous enstatite are shorter than the lifetime of disk gas (1–10 Myr; Pascucci and Tachibana 2010 and references therein) at temperatures above ~550–650 K for 0.1 μm- and 1 μm-sized grains (Fig. 6). This temperature range is close to those for amorphous forsterite (~500–600 K).

Water supply from vapor would be responsible for the isotopic exchange reaction at higher temperatures and lower P_{H2O} as in the case of amorphous forsterite. The value of β for amorphous enstatite in Eq. (2.3) was not derived from the present experiments, but it could be similar to that for amorphous forsterite ($\beta \sim 7.4 \times 10^{-6}$). The blue dashed curves in Fig. 2.12 show the calculated timescales of the water supply-controlled oxygen isotope exchange reaction with amorphous enstatite for α = 0.99 at $P_{\mathrm{H2O}} = 10^{-1}$ and 10^{-4} Pa with $\beta \sim 7.4 \times 10^{-6}$. It can be seen that the water supply from vapor would control isotope exchange reaction of amorphous enstatite at >1200 and 850 K at $P_{\mathrm{H2O}} = 10^{-1}$ and 10^{-4} Pa, respectively (Fig. 2.12), if the grains remain amorphous.

Crystallization timescale of amorphous enstatite for crystalline fraction of 0.99 was also evaluated from experimental data reported by Murata et al. (2009), and is shown as dotted-dashed curves in Fig. 2.12. The crystallization timescale at >~1000 K is shorter than the oxygen isotope exchange timescale controlled either by water diffusion or water supply (Fig. 2.12). Amorphous enstatite grains thus crystallize without effective oxygen isotope exchange if they were heated rapidly at >~1000 K, and further oxygen isotope exchange of crystalline enstatite with water vapor would occur between crystalline enstatite and water vapor.

The timescales of oxygen self-diffusion in 0.1 and 1 μm-sized crystalline diopside ($CaMgSi_2O_6$) grains are obtained using a reported diffusion coefficient (Ryerson and McKeegan, 1994) as an analogue of crystalline enstatite (long-dashed curves in Fig. 2.12) because no Arrhenius data for oxygen self-diffusion in crystalline enstatite has been reported. The timescale for oxygen self-diffusion in crystalline enstatite is smaller than or comparable to a disk gas lifetime at temperatures higher than ~1000 K (Fig. 2.12). Thus, oxygen isotope exchange reaction would occur with enstatite grains that are rapidly crystallized at >1000 K within the disk lifetime.

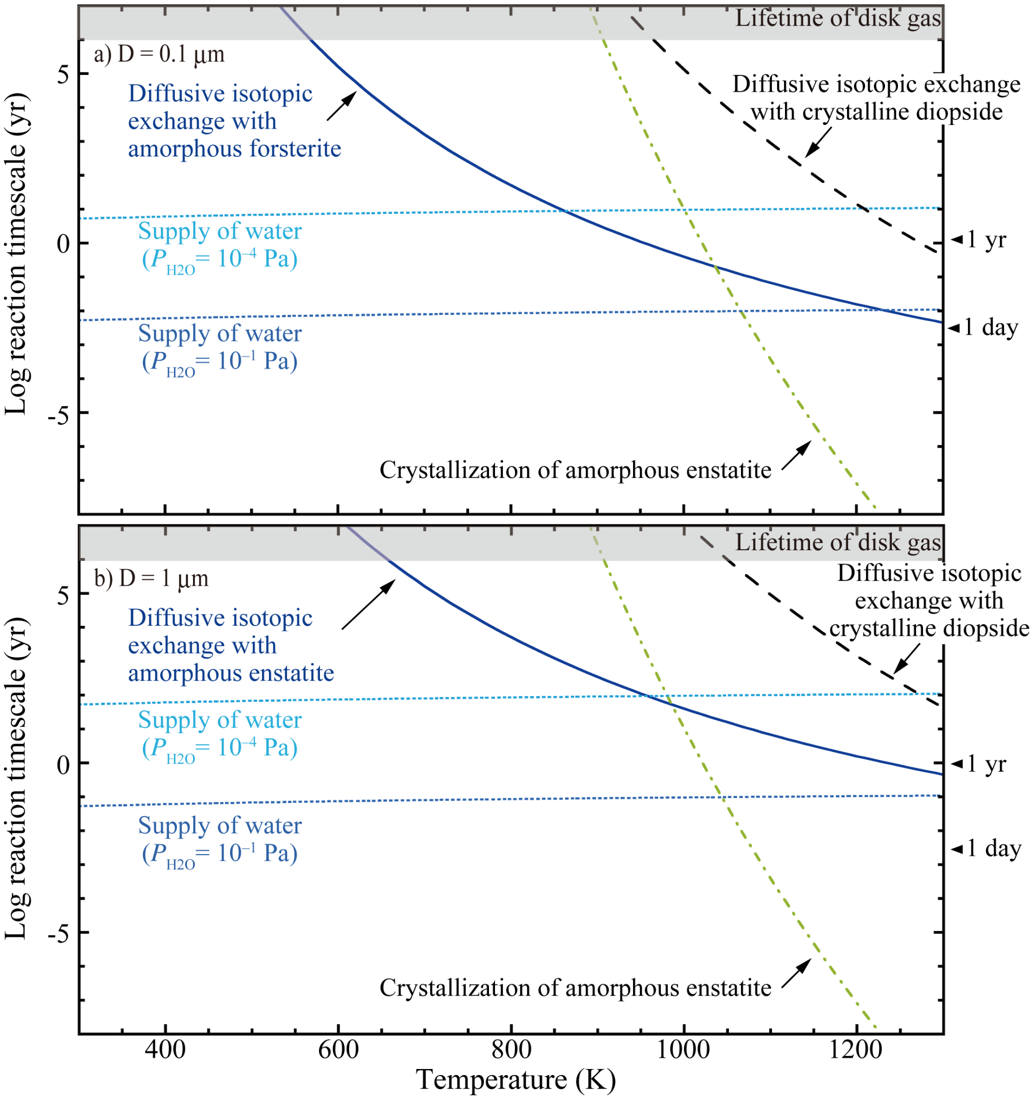

Fig. 2.12. Timescales of oxygen isotopic exchange between amorphous enstatite dust and water vapor in protoplanetary disks controlled by the diffusive isotopic exchange reaction (blue solid curves) and by the supply of water molecules at P_{H2O} of 10^{-1} and 10^{-4} Pa (blue dotted curves). Timescales of oxygen self-diffusion in crystalline diopside as an analogue of crystalline enstatite (black long dashed curves; Ryerson and McKeegan, 1994) and of crystallization of amorphous enstatite (green dot-dashed curves; Murata et al., 2009) are shown for comparison. The estimated lifetime of protoplanetary disk gas (1–10 Myr) is also shown for comparison. (a) 0.1 µm. (b) 1 µm.

In summary, amorphous forsterite and enstatite dust with a grain diameter up to ~1 μm would exchange oxygen isotopes with surrounding disk water vapor at temperatures higher than ~500–650 K within the lifetime of disk gas. Therefore, the original isotopic signatures of amorphous silicate grains would be erased when they were kept at >500–650 K in the protosolar disk. Most extraterrestrial samples available for measurements in laboratories (e.g. chondrules, chondrite matrix, interplanetary dust particles, and cometary silicate dust) is ^{16}O-poor isotopic compositions compared with calcium-aluminum-rich inclusions and amoeboid olivine aggregates (Kunihiro et al., 2005; McKeegan et al., 2006; Nakamura et al., 2008; Aléon et al., 2009; Krot et al., 2009 and references therein). Because silicate dust is primitive building blocks of those samples, most of primitive silicate dust would be thermally annealed at temperatures above ~500–650 K and experience oxygen isotopic exchange reaction in a ^{16}O-poor environment if primitive silicate dust was initially ^{16}O-rich.

Oxygen isotopic exchange reaction between amorphous silicate grains with forsterite and enstatite compositions and disk water vapor would also play an important role in diminishing the anomalous oxygen isotopic signature of presolar silicate grains. Silicate dust with olivine and pyroxene-like compositions were identified as abundant presolar silicates (Nguyen and Zinner, 2004; Nagashima et al., 2004; Floss and Stadermann, 2009; Vollmer et al., 2013), and those presolar silicate grains are typically up to 1 μm in size (Messenger et al. 2003; Nagashima et al., 2004; Hoppe, 2008; Floss and Stadermann, 2009; Floss and Stadermann, 2012; Leitner et al. 2012; Zinner, 2014; Hoppe et al. 2015). Moreover, crystalline silicate grains formed in circumstellar regions and subsequently incorporated into interstellar medium would be rendered amorphous by intense ion irradiation mostly coming from supernova shock waves (Demyk et al. 2001; Jones and Nuth, 2011), resulting in the lack of crystalline silicates in the interstellar medium (Kemper et al., 2004). Because those amorphous silicates were finally brought into the protosolar disk as the original Solar System ingredients, it is expected that original presolar silicates entering into the protosolar disk were dominantly in the amorphous form. Therefore, the temperatures of 500–650 K estimated in this study would be regarded as critical survival temperatures of presolar silicate grains in the protosolar disk before incorporation into planetesimals. The evidence of disk thermal destruction of oxygen isotopic signature of presolar silicate grains would be given by the low abundances of presolar silicate grains even in least altered carbonaceous chondrites, micrometeorites and anhydrous interplanetary dust particles ranges from ~100 to ~500 ppm (Floss & Haenecour 2016). Floss and Stadermann (2012) also showed that heterogeneous distribution of presolar silicates (and oxides) in a matrix of ungrouped carbonaceous chondrite Adelaide would be responsible for disk thermal processes.

2.6 *Conclusions*

Kinetics of oxygen isotopic exchange reaction between submicron-sized amorphous silicate grains with forsterite and enstatite compositions and water vapor under protoplanetary disk-like low P_{H2O} conditions was experimentally investigated. The amorphous samples were heated at 803−1123 K for 0−408 hours at 0.3 or 0.01 Pa of $H_2{}^{18}O$ (or $H_2{}^{16}O$) vapor.

At P_{H2O} of 0.3 Pa, diffusive oxygen isotopic exchange reaction between amorphous silicate and water vapor proceeded at 803–883 K with a diffusive isotopic exchange rate of D ($m^2\ s^{-1}$) = $(1.5 \pm 1.0) \times 10^{-19}\ \exp[-161.5 \pm 14.1\ (kJ\ mol^{-1})\ R^{-1}\ (1/T-1/1200)]$ for amorphous forsterite and at 923–1003 K with D ($m^2\ sec^{-1}$) = $(5.0 \pm 0.2) \times 10^{-21}\ \exp[-161.3 \pm 1.5\ (kJ\ mol^{-1})\ R^{-1}\ (1/T-1/1200)]$ for amorphous enstatite. Both crystallization and oxygen isotopic exchange of amorphous forsterite proceeded in parallel at 953 K and P_{H2O} of 0.3 Pa. Crystallization of amorphous forsterite dominated over oxygen isotopic exchange at 1073 K and P_{H2O} of 0.3 Pa, and no oxygen isotopic exchange was observed. This is because the crystallization rate is faster than the isotopic exchange rate at higher temperatures and because the isotopic exchange between crystalline forsterite and water vapor is more sluggish than that for amorphous forsterite.

At P_{H2O} of 0.01 Pa, the isotopic exchange between amorphous forsterite and water vapor at 853 and 883 K proceeded at the almost identical rate, which can be explained by the reaction controlled by the supply of water molecules. On the other hand, the reaction with amorphous forsterite at 803 K and P_{H2O} of 0.01 Pa was controlled by the diffusive exchange reaction as at P_{H2O} of 0.3 Pa because the diffusive exchange reaction becomes slower than the supply of water molecules at lower temperatures due to its larger temperature dependence.

Under T-P_{H2O} conditions in protoplanetary disks, the diffusive oxygen isotopic exchange reaction could be responsible for the oxygen isotopic evolution of amorphous silicate dust at lower temperatures, while the supply of water molecules from the vapor phase could control the oxygen isotopic exchange reaction at higher temperatures. However, when amorphous silicate crystallized rapidly at such high temperatures, the oxygen isotopic exchange would be controlled by oxygen self-diffusion in crystalline silicates, and the required timescale for oxygen isotopic exchange would become longer significantly than that for amorphous silicate.

The diffusive isotopic exchange rates for amorphous forsterite and enstatite indicate that oxygen isotopic exchange reaction between amorphous silicate dust and water vapor could proceed within a lifetime of protoplanetary disk gas (1−10 Myr) at temperatures above 500−650 K, and that the original isotopic signatures of primordial Solar System silicate and presolar silicate grains would be erased if the dust was kept at temperatures above 500−650 K in the early Solar System.

Chapter 3

3. Oxygen isotopic exchange kinetics between calcium-aluminum-rich inclusion melt and water vapor

3.1 *Introduction*

Calcium-aluminum-rich refractory inclusions (CAIs) are submillimeter- to centimeter-sized high temperature mineral assemblages, and are known as the oldest objects in the Solar System (Grossman 1972; Amelin et al., 2002; MacPherson, 2003; Connelly et al., 2012). Therefore, they record information on the high temperature thermal history at the earliest epoch of the Solar System. Type B CAIs are the most extensively studied sub-type of coarse-grained CAIs, and are composed of mainly spinel, melilite, fassaite, and anorthite (Grossman, 1980). They are not considered to be simple refractory condensates from the hot nebular gas, but are believed to experience multiple melting stages after the condensation of their precursors (e.g. MacPherson, 2003 and references therein; Yurimoto et al., 1998; Yoshitake et al., 2005; Kawasaki et al., 2018). Based on the thermodynamical calculation of equilibrium condensation from the hot nebular gas of the Solar System and the crystallization experiments of type B CAI analogues (Grossman 2000; Stolper & Paque, 1986; Paque et al., 2000), the formation scenario of type B CAIs is predicted as follows; the CAI precursor condensed from the hot solar nebular gas, and then experienced reheating events with a maximum temperature of ~1400–1550°C with subsequent cooling that causes the crystallization of melilite, followed by fassaite and anorthite.

Oxygen isotope measurements of CAIs have been extensively carried out since the first discovery of oxygen isotopic anomalies in Allende CAIs (Clayton et al., 1973), and oxygen isotopic compositions of coarse-grained CAIs exhibit heterogeneous oxygen isotopic distributions along the line with a slope of almost unity on the three-oxygen isotopic diagram. This oxygen isotopic variation cannot be explained by the mass-dependent isotopic fractionation, but could be due to mixing between isotopically distinct reservoirs (chapter 1). In typical type B CAIs, spinel and fassaite are ^{16}O-rich while anorthite and melilite are ^{16}O-poor (e.g. Clayton et al., 1977; Yurimoto et al. 1998; Yoshitake et al., 2005; Aléon, 2016; Kawasaki et al., 2018). The mechanism to produce the mineralogically controlled mass-independent oxygen isotopic variation among CAI constituent minerals is still controversial, but several mechanisms have been proposed (Clayton et al., 1977; Clayton, 1993; Yurimoto et al., 1998; Wasson et al., 2001; Ito et al., 2004; Yoshitake et al., 2005; Aléon, 2016; Kawasaki et al., 2018; Aléon, 2018). A possible explanation of the oxygen isotopic variations in CAIs is the partial melting and associated gas-melt oxygen isotopic exchange during reheating events (Clayton, 1993; Yurimoto et al., 1998; Ito et al., 2004; Yoshitake et al., 2005; Aléon, 2016; Kawasaki et al., 2018). The abrupt change in oxygen isotopic compositions within a single crystal of melilite found in Allende meteorites and progressive change of oxygen isotopic compositions of fassaite during its crystallization are also indicative of the oxygen isotopic exchange of partially melted CAIs with surrounding disk gas with different oxygen isotopic compositions (Yurimoto et al., 1998; Ito et al., 2004; Aléon, 2016; Kawasaki et al., 2018). Kawasaki et al. (2018) discussed timescales of oxygen isotopic exchange between a partially molten CAI droplet and disk gas during the fassaite crystallization with a plausible range of oxygen isotopic exchange efficiency (α) and reported diffusion coefficients of oxygen (D) in CAI-like melt (Oishi et al., 1974), but because of the lack of appropriate kinetic data for oxygen isotope exchange between CAI melt and disk gas, more detailed discussion on the oxygen isotopic evolution of CAI melt has not been conducted yet.

In the case of chondrules that also experienced melting process(es) in disk gas, experimental simulations of oxygen isotopic exchange between chondrule melts and water vapor have been carried out (Yu et al., 1995; Di Rocco & Pack, 2015). However, all their experiments were conducted at higher P_{H2O} compared with that in the protosolar disk, and simple extrapolation of experimental data to lower pressures may not be realistic or may require many assumptions. Therefore, oxygen isotopic exchange experiments between CAI/chondrule melts and disk gas should be carried out at protosolar disk-like low pressures of oxygen-bearing gas.

Water vapor is one of the most abundant reactive oxygen-bearing gas species in the protosolar disk. In this study, in order to reveal oxygen isotopic exchange kinetics and mechanism between CAI melt and disk gas, I conducted oxygen isotopic exchange experiments between CAI analogues with a type B CAI-like chemical composition and water vapor at protoplanetary disk-like low P_{H2O}, and report oxygen isotopic exchange kinetics to investigate the thermal history of CAIs in the earliest Solar System.

3.2 *Experiments*

Preparation of starting material

The composition of CAI droplet used in this study was close to the average Type B CAI composition (called as CAIB hereafter) (Wark, 1979). It is also close to the composition of CAIB of Stolper (1982) and Stolper and Paque (1986). The starting material was prepared by careful weighting of reagent powder of SiO_2, TiO_2, Al_2O_3, MgO and $CaCO_3$ with the weight fractions of 31.16, 1.12, 28.35, 10.12, and 29.24 wt%, respectively, and this mixture was ground in an agate mortar under ethanol for 1 hour. After drying the mixture in air at the room temperature, it was put in a platinum crucible and heated at 1000°C for 10 hours in order to decompose $CaCO_3$ into CaO. The heated powder put in a platinum crucible was again heated at 1525°C in a vertical 1 atm Keramax electric resistance furnace (Nikkato Corporation TS-4B06) for 24 hours and was subsequently quenched in air. The sample temperature of the Keramax furnace was checked by the melting points of gold (1064°C) and palladium (1555°C). The resulting material was composed of mainly glass with a small amount of spinel. Glass and spinel mixtures were ground in an alumina mortar for 30 minutes, and ground products (~0.03 g) were then shaped into cylindrical pellets (3 mm in outer diameter and 3 mm in thickness with a 1 mm-diameter inner hole). A 2.5 mm-diameter platinum wire loop with 5 mm-length platinum hook was prepared and weighted before the all the experiments. A sample pellet was then loaded above the platinum wire loop through the hook in order that samples sag into the wire loop by melting and stay there during experiments. The loaded samples were heated at 1500°C for 18 hours and was subsequently quenched in air. The spherical CAIB samples (starting material) were a glass and spinel mixture, and the glass composition of the CAIB samples is shown in Table 3.1. I also conducted isothermal experiments in air by using the sample pellet suspended above a platinum wire loop at 1350–1430°C for ~12 hours for determination of the liquidus temperature of melilite in the CAIB samples and for comparison with the samples heated under a controlled P_{H2O} as described in detail below. The liquidus temperature of melilite was determined to be ~1380°C, which is consistent with previous experiments with CAIB melt (~1400°C in Stolper, 1982; ~1410°C in Mendybaev et al., 2006).

Oxygen isotopic exchange experiments

Isothermal oxygen isotopic exchange experiments between CAIB melt and ^{18}O-enriched water vapor were conducted at 1390°C under the protosolar disk-like low P_{H2O} of 5×10^{-2} Pa for 3–24 hours using a spot-focus infrared gold image vacuum furnace (Advance-Riko MR 39H) equipped with a gas flow system for water vapor (Fig. 3.1). The furnace consists of a transparent silica glass tube (2.6 cm in inner diameter and 14.2 mm in length), double gold-coated ellipsoidal mirrors with two halogen lamps, a Pirani/cold-cathod vacuum gauge (Pfeiffer PKR251), a quadrupole mass spectrometer (QMS; HORIBASTEC QL-SG01-065-1A), a pumping system (a turbo-molecular pump and a scroll pump; HiCube 80 Eco, Pfeiffer Vacuum), a butterfly valve, a mass flow controller (Kofloc Model 3660), and a gas inlet for $H_2{}^{18}O$ vapor that is connected to a hydrogen gas cylinder. The CAIB glass made in air at 1500°C was weighted together with the platinum wire loop before an experiment, was suspended with the platinum hook on iridium wire above an iridium sample cell, which was located at the top of a type K thermocouple. The sample cell has a cylindrical shape with four 1 mm-diameter holes on the wall in order to let gas flow into the sample cell. Infrared light radiated from halogen lamps was focused on the sample cell by the double gold-coated ellipsoidal mirrors to heat the CAIB sample and surrounding flow gas simultaneously. The furnace temperature was monitored and controlled by the type K thermocouple. Because the location of the thermocouple is not exactly the same as the sample inside the sample cell, the temperature difference was corrected at $P_{H2O} = 5 \times 10^{-2}$ Pa using the liquidus temperature of melilite of the sample. The experiments at $P_{H2O} = 5 \times 10^{-2}$ Pa

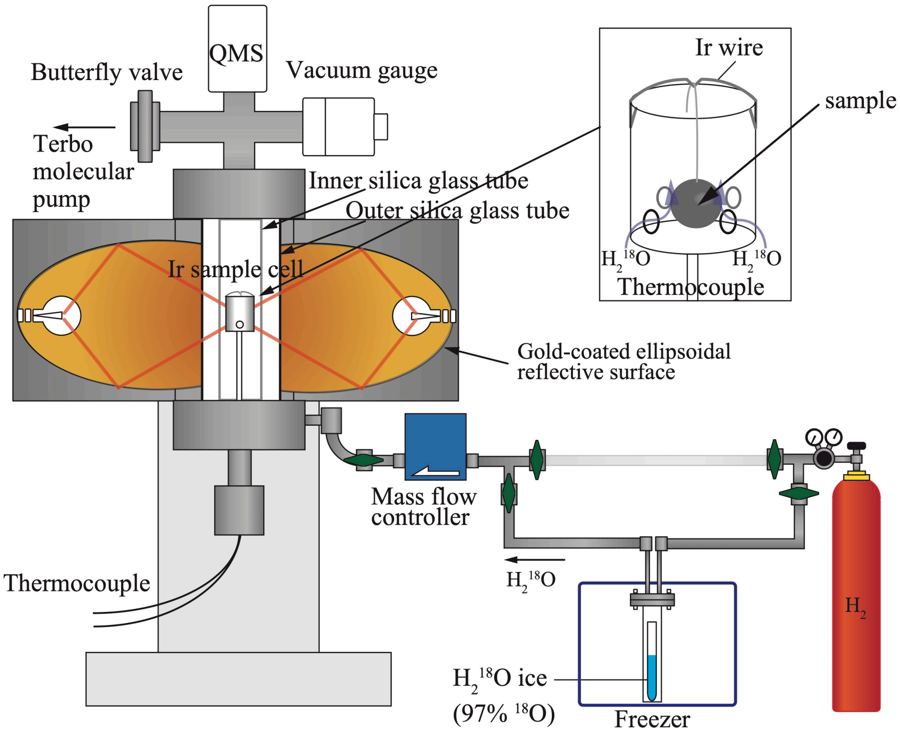

Fig. 3.1. Schematic illustration of the configuration of the spot focused infrared gold image vacuum equipped with a gas flow system for water vapor

were conducted at a temperature 10 K higher than the melilite liquidus temperature and the CAIB samples are expected to be composed of melt and spinel during the experiments. The pressure in the furnace was monitored by the Pirani/cold-cathod vacuum gauge. The gas species during the experiments was monitored by the quadrupole mass spectrometer.

Liquid reagent of $H_2{}^{18}O$ (97-atom% ^{18}O; Sigma-Aldrich) put in a silica glass container was sealed into a stainless container, and the stainless container was then connected to the hydrogen cylinder attached at the end of the gas flow line with the stainless tube. The inside of the stainless container was purged by hydrogen gas (>99.99% H_2) with the pressure of ~1.5–2 bars to eliminate the contribution of $H_2{}^{16}O$ permeating from the ambient gas, and liquid $H_2{}^{18}O$ in the stainless container was then frozen at –10°C in a freezer. The water ice was used as a water vapor source (Yamamoto and Tachibana, 2018; Yamamoto et al., 2018). After setting a CAIB sample in the iridium sample cell, the valve attached between the stainless container and the hydrogen cylinder was closed, and the mass flow controller was set to be fully opened. After the whole system was evacuated by the pumping system and P_{H2O} stabilized at the room temperature, the CAIB sample was pre-heated for 1 hour at temperatures of ~200–300°C and 700–800°C, which were much below solidus temperature of CAIB composition (~1230°C; Stolper, 1982), respectively, to reduce the contribution of adsorbed $H_2{}^{16}O$ vapor, and oxygen isotopic exchange between the CAIB melt and $H_2{}^{18}O$ vapor would not occur during the pre-heating treatment. The temperature of the CAIB sample was then rapidly increased to the maximum temperatures (1390°C) for 4 minutes in order to prevent the oxygen isotope exchange of CAI sample with $H_2{}^{18}O$ vapor during the heat-up period. The pressure inside the furnace was adjusted at 5×10^{-2} Pa by the butterfly valve after the sample temperature reached the maximum temperature, and the abundant gas species during the experiments were $H_2{}^{18}O$ and $H_2{}^{16}O$ vapor based on the QMS analysis, meaning that the total pressure inside the furnace is almost equal to P_{H2O}. The CAI sample was heated for desired duration (3–24 hours), and was then rapidly cooled down below the CAIB solidus temperature in a minute. After the experiments, the flow rate of the mass flow controller was set to be zero and the inside of the $H_2{}^{18}O$ stainless container was purged by hydrogen gas until the next experiment to eliminate the contamination of $H_2{}^{16}O$ from the ambient gas. Experimental conditions and results are summarized in Table 3.1.

Table 3.1. Experimental conditions and results of CAIB samples heated in air and $P_{H2O} = 5 \times 10^{-2}$ Pa.

Atmosphere	Temperature (K)	Duration (hour)	Weight of samples (g)	Diameter (cm)	Glass composition (wt%)						Spinel fraction (wt%)	
					MgO	Al_2O_3	SiO_2	CaO	TiO_2[b]	Σ	MgO[c]	Al_2O_3[c]
air	1500[a]	18	/	/	8.83	26.30	31.71	30.28	1.16	98.29	6.59	4.52
air	1390	12	/	/	7.47	22.89	35.20	32.40	1.28	99.22	12.72	11.20
air	1390	12	/	/	7.51	22.94	35.16	32.69	1.24	99.54	12.54	11.10
$H_2{}^{18}O$	1390	3	0.027	0.248	7.84	23.11	34.82	33.42	1.29	100.47	11.14	10.79
$H_2{}^{18}O$	1390	5	0.029	0.263	7.69	22.73	35.01	33.72	1.29	100.44	11.76	11.49
$H_2{}^{18}O$	1390	8	0.028	0.267	7.76	23.01	35.07	33.54	1.28	100.65	11.46	10.98
$H_2{}^{18}O$	1390	12	0.029	0.264	7.73	22.75	34.93	33.70	1.27	100.38	11.62	11.45
$H_2{}^{18}O$	1390	24	0.028	0.254	7.71	23.22	34.92	33.53	1.31	100.70	11.68	10.58

Notes

[a] Starting material for experiments at $P_{H2O} = 5 \times 10^{-2}$ Pa.

[b] Calculated with an assumption that all titanium is tetravalent.

[c] Calculated by the mass balance of proportion of MgO and Al_2O_3 between the bulk composition of the starting material and glass compositions in heated samples.

Analysis

Run products and the starting material, mounted into epoxy resin, were polished to expose the center of spherical CAIB samples to the surface with diamond plates, and then they were carefully polished by aluminum polishing papers (down to 0.5 micron). The cross sections were analyzed using a filed emission scanning electron microscope (FE-SEM; JEOL JSM-7000F) with an energy-dispersive X-ray spectrometer (EDS). The chemical compositions of glass in the starting material and run products were determined as an average composition of 14–25 spot analyses with 0.8 nA electron beam at an acceleration voltage of 15 kV for a quantitative elemental analysis.

The oxygen isotopic compositions were measured with a secondary ion mass spectrometry (SIMS; Cameca ims-1280HR) with a focused $^{133}Cs^+$ beam (20 keV, 0.5 nA) rastered over a 20 × 20 μm^2 area for 30–60 seconds for presputtering. The raster size of the primary beam was then reduced to 10 × 10 μm^2 and data was collected for 10–200 seconds. Negative secondary ions ($^{16}O^-$ and $^{18}O^-$) were measured simultaneously in the multi-collection mode using two Faraday cups with 10^{10} Ω resisters. The magnetic field was controlled by a NMR probe. The mass resolution of $M/\Delta M$ was set at ~2000. A normal incident electron flood gun was used for the electrostatic charge compensation of the analyzed area during the measurements. The background of the Faraday cup detectors was measured during presputtering of each analysis. Russian spinel ($\delta^{18}O$ = 8.5 ‰ relative to SMOW; Yurimoto et al., 1994) was used as a standard to correct instrumental mass fractionation. Reproducibility of measured $^{18}O/(^{16}O + ^{18}O)$ of Russian spinel is typically ~0.2 % (1-sigma standard deviation of the mean). An oxygen isotopic composition profile from a surface to an opposite surface passing through the center of the spherical sample was obtained with a step of ~20–50 μm.

After the SIMS analysis, the samples were observed with SEM to measure the distances of the analytical craters from the sample surface.

3.3 *Results and discussion*

The starting materials for oxygen isotopic exchange experiments are ~2.5–2.6 mm diameter spherical droplets, and consist of chemically homogeneous glass and spinel with a typical grain size <~20 μm in diameter (Fig. 3.2). Spinel was heterogeneously distributed along the platinum wire loop and at the top/bottom portion of the starting materials. The CAIB samples heated with $H_2{}^{18}O$ vapor were 2.5–2.6 mm-diameter spherical droplets, and were composed of glass and spinel with <~50 μm in diameter. Other crystalline phases such as melilite that is the second phase crystallizing from the CAIB melt (Stolper, 1982; Stolper & Paque, 1986) were not observed. Spinel crystals tend to exist at the bottom of the CAIB samples near the platinum wire loop. It was also observed that the amount and the size of spinel crystals in the CAIB samples heated with $H_2{}^{18}O$ vapor increased from the starting materials. This is because the heating/quenched temperature in air for preparing the staring

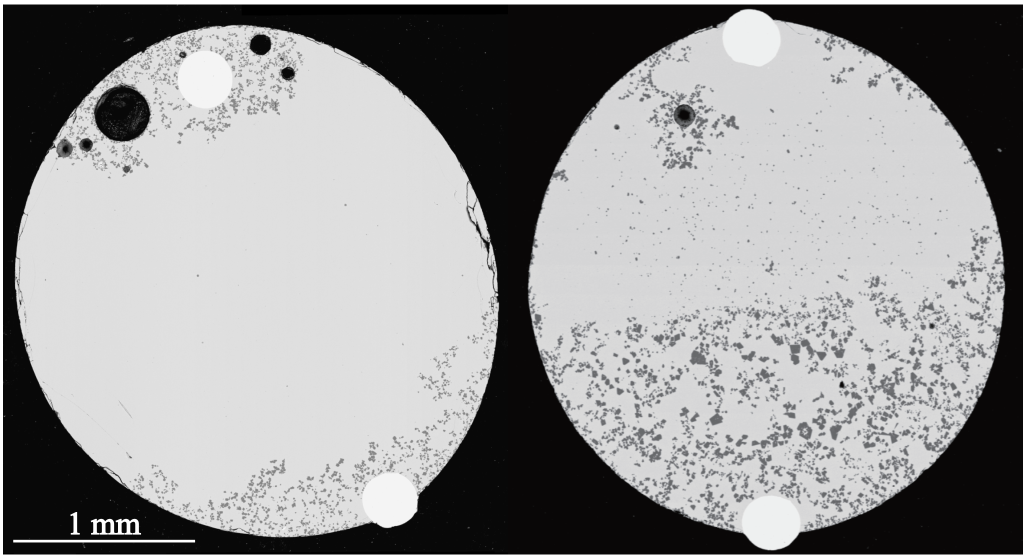

Fig. 3.2. Backscattered electron (BSE) images of the starting material heated at 1500°C for 18 hours in air (*left*) and of the samples heated at 1390°C for 5 hours at $P_{H2O} = 5 \times 10^{-2}$ Pa (*right*). The regions with brighter and darker contrasts are glass and spinel, respectively.

material (1500°C) is higher than that of oxygen isotopic exchange experiments (1390°C), resulting in crystallization of spinel at the experimental temperature (Stolper & Paque, 1986). However, the amount of spinel remained constant after 3 hour-heating due to rapid crystallization of spinel, and the change of melt composition due to spinel crystallization would be completed with a shorter timescale than the isotope exchange.

The chemical compositions of glass and the amount of coexisting spinel in the CAIB samples heated at 5×10^{-2} Pa of $H_2{}^{18}O$ vapor and in air at 1390°C are shown in Table 3.1. The amount of spinel was calculated by the mass balance of proportion of MgO and Al_2O_3 between the bulk composition of the starting material and glass compositions in heated samples assuming that no evaporation occurred from the melt. The glass compositions of samples heated with $H_2{}^{18}O$ vapor were consistent with that heated in air at the same heating temperature of 1390 °C. The amount of spinel in samples heated with $H_2{}^{18}O$ vapor (~11–12 wt%) was also consistent with that in samples heated in air. Because little or no evaporation of CAIB melt occurs in air (Mendybaev et al., 2006), these evidences suggest that significant evaporation of moderately volatile elements (e. g. magnesium and silicon; Mendybaev et al., 2006) from the CAIB melt did not occur at 5×10^{-2} Pa of $H_2{}^{18}O$ vapor, and the melt compositions did not change through oxygen isotopic exchange experiments.

Figure 3.3 shows the spatial distributions of oxygen isotopic composition, normalized to that of water vapor, ($f^{18}O / f^{18}O_w$) in glasses heated for different durations, where $f^{18}O$ is $^{18}O/(^{16}O + {}^{18}O)$ of the sample and $f^{18}O_w$ is that of water vapor. The value of $f^{18}O_w$ was estimated to be ~0.91 by QMS analysis of gas in the furnace during a blank experiment at the same temperature and P_{H2O}. If a sample equilibrates isotopically with the ambient water vapor, $f^{18}O / f^{18}O_w$ should be equal to 1. The ^{18}O fraction increases toward the surface of the sphere. In addition, the fraction of ^{18}O at the surface of the sphere is not the same as that of water vapor even for samples heated for 24 hours, but gradually increases with time. The spatial distribution of oxygen isotope composition and its temporal change suggest that the surface oxygen isotopic exchange

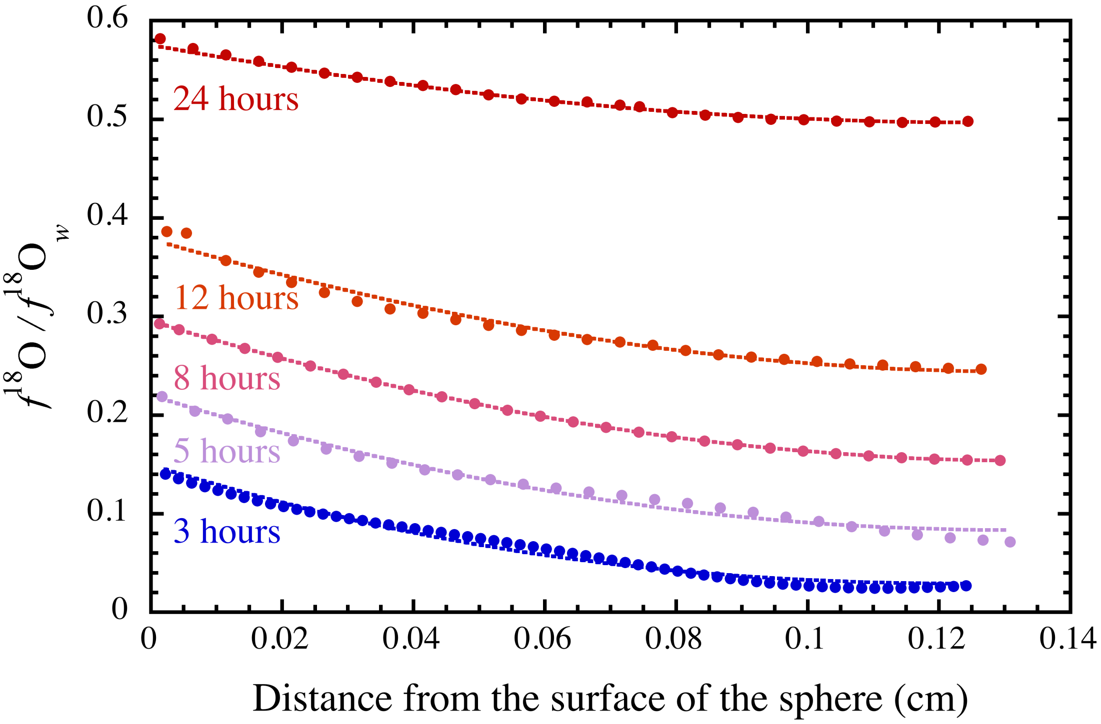

Fig. 3.3. Typical profiles of normalized oxygen isotopic compositions of glass in samples heated at $P_{H2O} = 5 \times 10^{-2}$ Pa for 3, 5, 8, 12, and 24 hours as a function of distance from the surface of the sphere. Dotted curves are best-fitted results by Eq. (3.2).

with surrounding water vapor and the oxygen self-diffusion in the CAI melt simultaneously proceeded.

The surface isotopic exchange flux is related to the difference between oxygen isotopic compositions at the surface and in the gas and the flux of oxygen across the surface $-D(\partial f^{18}O/\partial r)_s$, the relation is given by (Crank, 1975);

$$-D\left(\partial f^{18}\mathrm{O}/\partial r\right)_s = k\left(f^{18}\mathrm{O}_s - f^{18}\mathrm{O}_w\right), \tag{3.1}$$

where k is the rate constant for the surface isotopic exchange, r is the distance from the center of the sphere, and $f^{18}O_s$ is the $f^{18}O$ at the surface. The solution of Eq. (3.1) is expressed as follows (Crank, 1975);

$$\frac{f^{18}\mathrm{O} - f^{18}\mathrm{O}_w}{f^{18}\mathrm{O}_i - f^{18}\mathrm{O}_w} = \frac{2La}{r}\left(-1\right)^n \frac{\exp\left(-D\beta_n^2 t/a^2\right)}{\left\{\beta_n + L\left(L-1\right)\right\}} \frac{\sin\beta_n r/a}{\sin\beta_n}, \tag{3.2}$$

The β_n's are the positive roots of

$$\beta_n \cot \beta_n + L - 1 = 0\,, \tag{3.3}$$

and L is a dimensionless parameter expressed as

$$L = ka/D\,, \tag{3.4}$$

where $f^{18}O_i$ is the initial value of $f^{18}O$ (i.e. 0.002), a is the diameter of the sphere, and t is time. The obtained oxygen isotopic profiles are well fitted with Eq. (3.2) (Fig. 3.3), and the values of D and k were independently evaluated (Fig. 3.4).

The obtained D as a function of heating duration is shown in Fig. 3.4a. Data is slightly scattered, but appears to be constant ($(1.87 \pm 0.53) \times 10^{-7}$ cm^2 sec^{-1} on average) irrespective of heating duration. The obtained D in CAIB melt is consistent with that estimated in basaltic melt at 1390°C (~ 1.7–1.8×10^{-7} cm^2 sec^{-1}) (Canil and Muehlenbachs, 1990; Lesher et al., 1996). This is likely because the diffusivity of oxygen would be related to the degree of melt polymerization (NBO/T) (Liang et al., 1996) and the CAIB melt has a similar NBO/T value of ~1.1 as that of basaltic melt (NBO/T~1). In contrast, the D at 1390°C in the melt with the $40CaO$-$20Al_2O_3$-$40SiO_2$ composition reported by Oishi et al. (1974) is approximately one order of magnitude larger than that estimated in this study (1.3×10^{-6} cm^2 sec^{-1}) although the melt composition and the NBO/T value (~1) in their study are close to those in this study. However, a more recent study by Liang et al. (1996) reported D that is one order of magnitude smaller than that of Oishi et al. (1974) at 1500°C for the same melt composition as Oishi et al. (1974). Therefore, I should refrain from comparing D in this study with that in Oishi et al. (1974).

Figure 3.4b shows the obtained k as a function of heating duration. The k is independent of heating duration, and is found to be $(4.23 \pm 0.3) \times 10^{-7}$ cm sec^{-1} on average. The k is described as follows using a non-dimensional parameter α that expresses the oxygen isotopic exchange efficiency of colliding water molecules at the surface of melt;

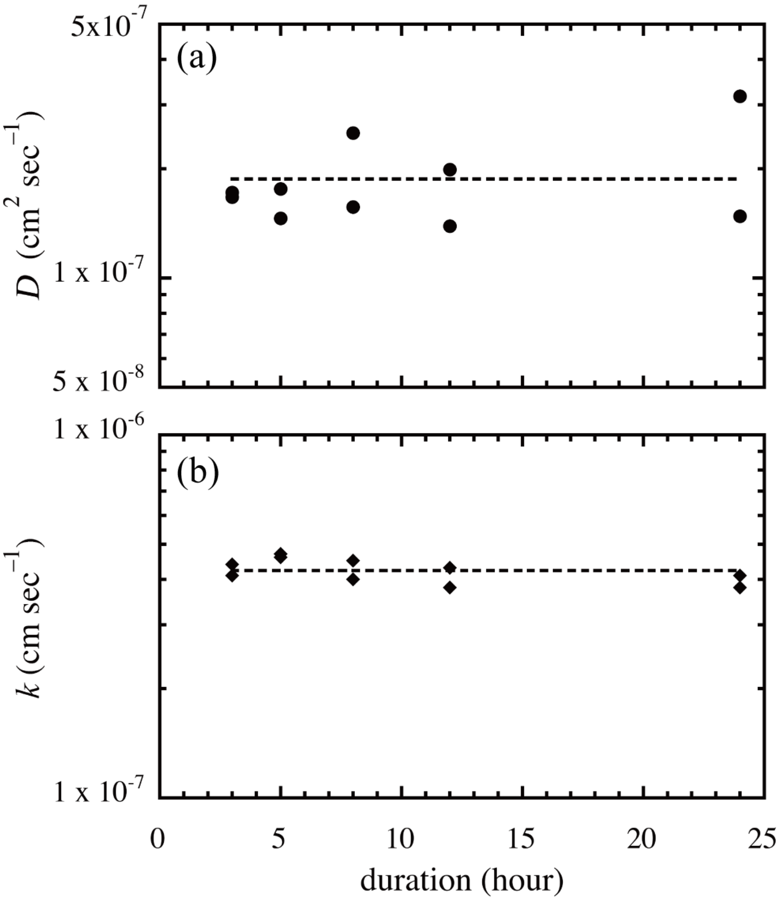

Fig. 3.4. (a) Oxygen diffusion coefficient D and (b) surface isotopic exchange rate k as a function of heating duration. Dotted lines are the average values of D and k.

$$k = \alpha J_w / C_{\mathrm{O}} \tag{3.5}$$

where J_w is the flux of water molecules as given by Eq. (2.1) (chapter 2), and C_{O} is the oxygen number density in the melt. C_{O} was calculated to be ~4.88 × 10^{22} (cm^{-3}) as an average considering the average proportion of spinel in samples as ~11.3wt% (Table 3.1). The α is estimated to be ~0.27, meaning that 27% of colliding water molecules to the melt surface exchange oxygen isotopes at the melt surface.

3.4 *Application to the thermal history of CAIs*

Melilite is the first phase crystallizing from spinel-bearing CAI melt with type B CAI composition (Stolper, 1982). Melillite in type B CAIs shows typically

^{16}O-poor oxygen isotopic compositions with a limited isotopic variation (McKeegan et al., 1996; Aléon, 2016; Kawasaki et al., 2018). Kawasaki et al. (2018) showed oxygen isotopic variation of melilite in a 1 cm-sized type B CAI is 1.3 ‰ in δ^{18}O of 3.1 ‰ (2-sigma standard deviation) in respective of their åkermanite contents and the location of melilite. If the precursors of CAIs had ^{16}O-rich isotopic compositions close to that of spinel ($\delta^{18}\mathrm{O} = -45.3$‰ in Kawasaki et al., 2018), those observations indicate that melilite crystallized from the melt that was isotopically equilibrated with surrounding disk gas with ^{16}O-poor isotopic compositions above the melilite liquidus temperature. Therefore I calculated time required to reach the isotopic exchange fraction of 97% as a function of P_{H2O} ($10^{-9} \le P_{\mathrm{H2O}}$ (bar) $\le 5 \times 10^{-4}$) at 1390°C for 1 mm- and 1 cm-sized partially molten CAI droplets because type B CAIs are sub-millimeter- to centimeter-sized objects (MacPherson, 2003; MacPherson et al., 2005; Simon et al., 2018). The timescale was evaluated by the modified form of Eq. (3.2) to express oxygen isotopic exchange fraction for bulk (Crank, 1975);

$$x_{dif.} = 1 - \sum_{n=1}^{\infty} \frac{6L^2 \exp\left(-\beta_n^2 Dt/a\right)}{\beta_n^2 \left\{\beta_n^2 + L\left(L-1\right)\right\}}, \tag{3.6}$$

where $x_{dif.}$ is the bulk exchange fraction. The value of L in Eq. (3.6) at a certain P_{H2O} was calculated by Eqs. (3.4) and (3.5). I also evaluated the timescale at 1540°C by estimating the oxygen diffusion coefficient at 1540°C with an assumption that the activation energy for oxygen self-diffusion in CAIB melt is equal to that in basaltic melt reported by Lesher et al. (1996) (170 kJ mol^{-1}) who reported the oxygen diffusion coefficient at 1390°C similar to that in this study. The temperature of 1540°C is 10 K lower than the experimentally-determined spinel liquidus of CAIB melt (Stolper, 1982), and the CAIB should be composed of melt and relict spinel at the temperature range of 1390–1540°C.

I also calculated the timescale of oxygen isotopic exchange reaction controlled only by the supply of water molecules. The supply-controlled oxygen isotopic exchange rate is expressed by

$$\frac{dx_{supply}}{dt} = \frac{\alpha J_w S\left(1 - x_{supply}\right)}{VC_{\mathrm{O}}} \quad (3.7)$$

where x_{supply} is the bulk isotopic exchange fraction when the oxygen isotopic exchange reaction is controlled by the supply of water molecules, S is the melt surface, and V is the melt volume. The integral expression of Eq. (3.7) is given by

$$x_{supply} = 1 - \exp\left(-\frac{\alpha J_w St}{VC_{\mathrm{O}}}\right) \quad (3.8)$$

Figures 5a and 5b show the timescales for exchange fraction of 99.5% in 1 mm- and 1 cm-sized CAI melt droplets calculated by Eqs. (3.6) and (3.8) as expressed by $t_{dif.}$ and t_{supply}, respectively. The timescale required for oxygen isotopic equilibrium between H_2O and CO (Alexander, 2004; J. R., Lyons, personal communication) and the timescale of oxygen self-diffusion in spinel with grain diameter of 10 μm at 1390 and 1540°C (Ryerson and McKeegan, 1994) are also shown comparison. The ratios of $t_{dif.}$ and t_{supply} are shown in Fig. 3c and 3d for 1 mm- and 1 cm-sized CAI melt droplets, respectively. The ratios of $t_{dif.}$ and t_{supply} correspond to ~1 at $P_{\mathrm{H2O}} \leq \sim 10^{-6}$ bar for 1 mm-sized droplet and at $P_{\mathrm{H2O}} \leq \sim 10^{-7}$ bar for 1 cm-sized droplet, suggesting that the oxygen isotopic exchange reaction is controlled by the supply of water molecules from gas at low P_{H2O}. In contrast, at higher P_{H2O}, $t_{dif.}$ is deviated from the lines of t_{supply} and shows almost constant values at $P_{\mathrm{H2O}} > \sim 10^{-4}$ bar for 1 mm-sized droplet and $P_{\mathrm{H2O}} > \sim 10^{-5}$ bar for 1 mm-sized droplet. This suggests that oxygen isotopic exchange is controlled by diffusion inside the melt at higher P_{H2O}. The transition from the supply-controlled reaction to the diffusion-controlled reaction occurs at higher P_{H2O} at 1540°C than that at 1390°C. This is because the supply-controlled reaction has weak temperature dependence as discussed in chapter 2 while the diffusivity increases with increasing temperature following the Arrhenius relation. The ratios of Ti^{3+} and Ti^{4+} in fassaite and hibonite in CAIs indicate that those minerals crystallized under reducing conditions, close to H_2O/H_2 ratio estimated from the Solar System abundance of elements (H_2/H_2O~10^3; Lodders, 2003), if they were in equilibrium with disk gas (Beckett, 1986; Beckett et al., 1988). Therefore, P_{H2O} of 10^{-6} and 10^{-9} bar would be the upper and lower limits of water vapor pressure during the formation of CAIs assuming that total pressure ranging from 10^{-3} and 10^{-6} bar (Wood and Morfill, 1988). If this was the case, the timescales required for CAI melts to equilibrate isotopically with disk gas would be mainly determined by the water supply-controlled reaction (Fig. 3.5), and the timescale does not differ significantly at temperatures from 1390°C to 1540°C. The time required for CAI melt to isotopically equilibrate with ambient water vapor is longer than ~30 hours for 1 mm-sized CAI and ~300 hours for 1 cm-sized CAI at P_{H2O} of 10^{-6}–10^{-9} bar. Therefore, type B CAIs (<1 cm) with homogeneous ^{16}O-poor compositions of melilite would be heated above the melilite liquidus for at least a dozen days in a ^{16}O-poor environment of the early Solar System. It is noted that CAIs would experience repeated heating processes (e.g. Yurimoto et al., 1998; Yoshitake et al., 2005; Kawasaki et al., 2018), and these estimated heating time would be regarded as the total heating duration. It is also noted that spinel grains in CAIs have uniformly ^{16}O-rich oxygen isotopic compositions, and relict spinel thus did not exchange oxygen isotopes with surrounding CAI melt during reheating processes (Kawasaki et al. 2018). Small spinel grains available for oxygen isotopic measurements by SIMS are typically 10 μm in size (2-3 μm-sized beam was used for measurements in Kawasaki et al. 2018). The timescales of oxygen self-diffusion in spinel with grain diameter of 10 μm at 1540 and 1390°C are ~1 and 10 years, respectively, and CAI melt should not have been kept at temperatures of 1540°C for ~1 year and 1390°C for ~10 years.

I note that the H_2O-CO equilibration timescales at 1390 and 1540°C are always shorter than the oxygen isotopic exchange timescales of CAI melt, suggesting that CAI melt would exchange oxygen isotopes with water vapor that already isotopically equilibrated with CO gas. If this was the case, homogeneous oxygen isotopic compositions of melilite in type B CAIs would reflect the bulk oxygen isotopic composition of disk gas before and during the melilite crystallization from CAI melt.

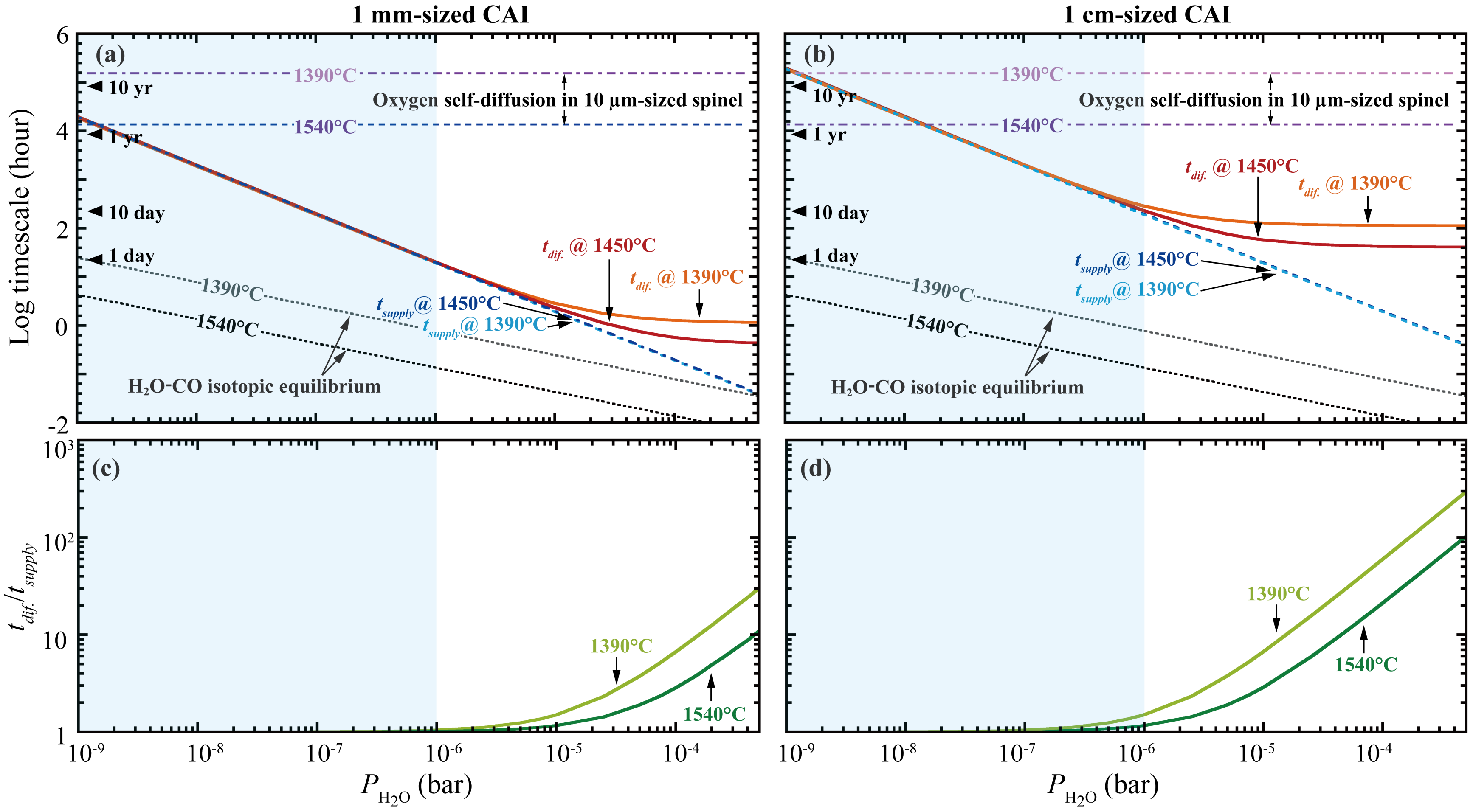

Fig. 3.5. Timescales of oxygen isotopic exchange between CAI melt with diameters of 1 mm and 1 cm [a, b] and water vapor at 1390 and 1540°C as a function of P_{H2O} for the exchange fraction of 97%. Dotted light and dark blue straight lines are t_{supply} estimated by Eq. (3. 8) at 1390 and 1540°C,

respectively, and solid orange and red curves are $t_{dif.}$ estimated by Eq. (3.6) at 1390 and 1540°C, respectively. The timescale required for oxygen isotopic equilibrium between H_2O and CO as a faction of P_{H2O} (Alexander, 2004; J. R., Lyons, personal communication) and the timescale of oxygen self-diffusion in spinel with grain diameter of 10 μm at 1390 and 1540°C (Ryerson and McKeegan, 1994) are also shown for comparison. Also shown in [c, d] are ratios of $t_{dif.}$ and t_{supply} at 1390 and 1540°C as a function of P_{H2O} for 1 mm- and 1 cm-sized CAI melt. Blue shaded area is a plausible range of P_{H2O} in the canonical protosolar disk (Beckett, 1986; Beckett et al., 1988; Wood and Morfill, 1988; Lodders, 2003)

3.5 *Conclusions*

Fundamental kinetic parameters for oxygen isotopic exchange of CAI melt with disk gas were obtained by conducting oxygen isotopic exchange experiments at 1390°C between silicate melt with a type B CAI-like composition and water vapor with a pressure of 5×10^{-2} Pa to discuss the thermal history of CAIs in the earliest epoch of Solar System evolution. The heated samples were composed of glass and spinel. The ^{18}O fraction in the melt increased toward the surface of the sphere, and that at the surface increased with time, suggesting that the surface oxygen isotopic exchange and the volume diffusion simultaneously proceeded. Obtained oxygen isotopic profiles were explained by a three-dimensional spherical diffusion equation with a time-dependent surface concentration, yielding the oxygen diffusion coefficient of 1.87×10^{-7} cm^2 sec^{-1} and the surface oxygen isotopic exchange efficiency of ~0.27 for colliding water molecules. At temperatures above the melilite liquidus and plausible partial pressures of water vapor in the protosolar disk, oxygen isotopic exchange reaction between CAI melt (<1 cm) and water vapor would be mainly controlled by the supply of water vapor, and time required for the melt to isotopically equilibrate with disk water vapor is at least ~300 hours for 1 cm-sized CAI melt. Homogeneous ^{16}O-poor oxygen isotopic compositions of melilite in most natural type B CAIs suggests that type B CAIs would be heated for at least a dozen days in total in a ^{16}O-poor environment during the (multiple) reheating processes in the early Solar System.

4. Summary and future works

The mass-independent oxygen isotopic fractionation of primitive extraterrestrial materials is an evidence of mixing between ^{16}O-rich and ^{16}O-poor reservoirs in the early Solar System. Oxygen isotopic exchange kinetics between amorphous silicate/calcium-aluminum-rich inclusions (CAIs) and disk water vapor were experimentally investigated under protosolar-disk like low water vapor pressure (P_{H2O}) conditions in this thesis.

Oxygen isotopic exchange between amorphous silicates and water vapor and its implications to oxygen isotopic evolution in the early Solar System: The oxygen isotopic exchange reaction rate is controlled either by the diffusive isotopic exchange in the amorphous structure or by the supply of water molecules from gas phase. The diffusive oxygen isotopic exchange rates are given by D (m^2 s^{-1})= (1.5 ± 1.0) × 10^{-19} exp[-161.5 ± 14.1 (kJ mol^{-1}) R^{-1} ($1/T - 1/1200$)] for amorphous forsterite and D (m^2 sec^{-1}) = (5.0 ± 0.2) × 10^{-21} exp[-161.3 ± 1.5 (kJ mol^{-1}) R^{-1} ($1/T - 1/1200$)] for amorphous enstatite. The supply-controlled isotopic exchange rate was also evaluated for amorphous forsterite. The kinetics indicates that original isotopic signatures of amorphous silicate dust with grain diameters up to 1 μm would be erased through oxygen isotopic exchange with disk water vapor within the lifetime of disk gas if the dust was kept at temperatures above ~500–650 K. The oxygen isotopic exchange reaction between amorphous silicate and water vapor would also determine the survivability of presolar oxygen isotopic signatures of silicate grains prior to the incorporation into planetesimals.

Oxygen isotopic exchange kinetics between calcium-aluminum-rich inclusion (CAI) melt and water vapor: The samples with a type B CAI-like composition heated at 1390°C and $P_{\mathrm{H2O}} = 5 \times 10^{-2}$ Pa for 3–24 hours were composed of melt and spinel. The ^{18}O-fraction in the melt increased toward the surface of the sphere, and that at the surface increased with time, suggesting that the surface isotopic exchange and the oxygen diffusion in the melt simultaneously proceeded. Obtained oxygen isotopic profiles were fitted with a three-dimensional spherical diffusion equation with a time-dependent surface concentration, yielding the oxygen diffusion coefficient of ~1.87×10^{-7} cm^2 sec^{-1} and the surface oxygen exchange efficiency of ~0.27 for colliding water molecules. According to the oxygen isotopic exchange kinetics in the protosolar disk, homogeneous ^{16}O-poor isotopic compositions of melilite in most natural type B CAIs indicate that type B CAIs would be heated for at least a dozen days in total during the reheating processes above the liquidus temperature of melilite in a ^{16}O-poor environment.

The findings described here are the first fundamental and quantitative kinetic data for oxygen isotopic exchange between primitive materials (amorphous silicate dust and CAIs) and disk water vapor demonstrated under disk-like low water vapor pressure conditions to constrain physical and chemical conditions of the protosolar disk. I found through this research that the experimental investigation of oxygen isotopic exchange kinetics between those primitive materials and CO gas (less reactive than H_2O though) will deepen our understanding of oxygen isotopic evolution of the Solar System more because ^{16}O-rich CO gas is another end component that would have been responsible for oxygen isotopic evolution of primitive extraterrestrial materials. This kinetics will be examined through the near future experiments with similar experimental techniques.

Acknowledgements

This Ph.D thesis benefited from many people who have contributed to this thesis directly or have provided helpful advice and suggestions.

Above all, I would like to express my gratitude to Professor Hisayoshi Yurimoto (Hokkaido University) and Professor Shogo Tachibana (University of Tokyo) for giving me a great opportunity to realize such a study and helpful and continuous suggestions and comments. I also would like to express my gratitude to Dr. Junji Yamamoto (Hokkaido University) for advices and valuable comments. I also would like to express my gratitude to Professor Takaya Nagai for giving me a helpful comments and advices and allowing me to use the Keramax electric furnace for CAI experiments.

I am grateful to Dr. Noriyuki Kawasaki and Ms. Minami Kuroda (Hokkaido University) for SIMS analysis of samples and related helpful suggestions and comments. I am also grateful to Professor Akira Tsuchiyama and Dr. Junya Matsuno (Kyoto University) for kindly providing amorphous powder, and Dr. James R. Lyons (Arizona State University) for the discussion of oxygen isotopic exchange between H_2O and CO. I would like to thank Ms. Michiru Kamibayashi (Hokkaido University) who significantly contributed to the CAI experiments, and Ms. Megumi Mori (Hokkaido University) who helped me with the calculation of the oxygen isotopic profiles in the CAI experiments. I also would like to thank Dr. Naoya Sakamoto and Dr. Ken-ichi Bajo (Hokkaido University) for insightful comments and suggestions.

Finally, I wish to give my thanks to all other staffs and students in the Geochemistry group in Hokkaido University. They were always giving me helpful support and advice.

This work was financially supported by a Grant-in Aid for JSPS Research Fellow (17J05044) and Ministry of Education, Sports, Science and Technology KAKENHI grant.

References

- Abe K., Sakamoto N., Krot A. N., and Yurimoto. H. 2017. Occurrences, abundances, and compositional variations of cosmic symplectites in the Acfer 094 ungrouped carbonaceous chondrites. *Geochemical Journal* 51: 3–15.
- Aléon J., Engrand C., Leshin L. A., and McKeegan K. D. 2009. Oxygen isotopic compositions of chondritic interplanetary dust particles: A genetic link between carbonaceous chondrites and comets. *Geochimica et Cosmochimica Acta* 73: 4558–4575.
- Aléon J. 2016. Oxygen isotopes in the early protoplanetary disk inferred from pyroxene in a classical type B CAI. *Earth and Planetary Science Letter* 440: 62–70.
- Aléon J. 2018. Closed system oxygen isotope redistribution in igneous CAIs upon spinel dissolution. *Earth and Planetary Science Letters* 482: 324–333.
- Alexander C. M. O'D. 2004. Chemical equilibrium and kinetics constrains for chondrule and CAI formation conditions. *Geochimica et Cosmochimica Acta* 68: 3943–3969.
- Amelin, Y., Krot A. N., Hutcheon, I. D., and Ulyanov, A. A. 2002. Lead isotopic ages of chondrules and calcium-aluminum-rich inclusions. *Science* 297: 1678–1683.
- Beckett J. R. 1986. The origin of calcium, aluminum-rich inclusions from carbonaceous chondrites: An experimental study. *PhD thesis*, University of Chicago.
- Beckett J. R., Live D., Tsay F.-D., Grossman L., and Stolper E. 1988. Ti3+ in meteoritic and synthetic hibonite. *Geochimica et Cosmochimica Acta* 52: 1479–1495.
- Canil D. and Muehlenbachs K. 1990. Oxygen diffusion in an Fe-rich basalt melt. *Geochimica et Cosmochimica Acta* 54: 2947–2951.

- Clayton R. N., Grossman L., and Mayeda T. K. (1973) A component of primitive nuclear composition in carbonaceous chondrites. *Science* 182: 485–488.
- Clayton R. N., Onuma N., Grossman L., and Mayeda T. K. 1977. Distribution of the pre-solar component in Allende and other carbonaceous chondrites. *Earth and Planetary Science Letters* 34: 209–224.
- Clayton R. N. 1993. Oxygen isotopes in meteorites. A*nnual Review of Earth and Planetary Science* 21: 115–149.
- Connelly J. N., Bizzarro M., Krot, A. N., Nordlund Å, Wielandt D., and Ivanova M. A. 2012. The absolute chronology and thermal processing of solids in the solar protoplanetary disk. *Science* 338: 651–655.
- Crank J. 1975. The Mathematics of Diffusion. 2nd edition Oxford: Oxford University Press.
- Demyk K., Carrez Ph., Leroux H., Cordier P., Jones A. P., Borg, J., Quirico E., Raynal P. I., and d'Hendecourt L. 2001. Structural and chemical alteration of crystalline olivine under low energy He^+ irradiation. *Astronomy & Astrophysics 368*: L38–L41.
- Di Rocco T. and Pack A. 2015. Triple oxygen isotope exchange between chondrule melt and water vapor: An experimental study. *Geochimica et Cosmochimica Acta* 164: 17–34.
- Fagan T. J., Krot A. N., Keil K., and Yurimoto H. 2004. Oxygen isotopic evolution of amoeboid olivine aggregates in the reduced CV3 chondrites Efremovka, Vigarano, and Leoville. *Geochimica et Cosmochimica Acta* 68: 2591–2611.
- Floss C. and Stadarmann F. 2009. Auger nanoprobe analysis of presolar ferromagnesian silicate grains from primitive CR chondrites QUE 99177 and MET 00426. *Geochimica et cosmochimica Acta* 73: 2415–2440.
- Floss C. and Stadermann F. J. 2012. Presolar silicate and oxide abundances and compositions in the ungrouped carbonaceous chondrite Adelaide and the K chondrite Kakangari: The effects of secondary processing. *Meteoritics & Planetary*

Science 47: 992–1009.

- Floss C. and Haenecour P. 2016. Presolar silicate grains: Abundances, isotopic and elemental compositions, and the effects of secondary processing. *Geochemical journal* 50: 3–25.
- Grossman L. 1972. Condensation in the primitive solar nebula. *Geochimica et Cosmcochimica Acta* 36: 597–619.
- Grossman K. 1980. Refractory inclusions in the Allende meteorites. *Annual Review of Earth and Planetary Sciences* 8: 559–608.
- Grossman L., Ebel D. S., Simon S. B., Davis A. M., Richter F. M., and Parsad N. M. 2000. Major element chemical and isotopic composition of refractory inclusions in C3 chondrites: The separate roles of condensation and evaporation. *Geochimica et Cosmochimica Acta* 64: 2879–2894.
- Henning Th. 2010. Cosmic silicates. *The Annual Review of Astronomy and Astrophysics* 48: 21–46.
- Hoppe P. 2008. Reservoir for comet material: Circumstellar grains. *The Space Science Reviews* 138: 43–57.
- Hoppe P., Leitner J., and Kodolányi J. 2015. New constrains on the abundances of silicate and oxide stardust from supernovae in the Acfer 094 meteorite. *The Astrophysical journal* 808: L9 (6pp).
- Imai Y. 2012. Experimental study of circumstellar silicate dust evolution by crystallization processes using laboratory infrared spectroscopy. *Ph.D Thesis*, Osaka University, Osaka, Japan
- Ito M., Nagasawa H., and Yurimoto H. 2004. Oxygen isotopic SIMS analysis in Allende CAI: Details of the very early thermal history of the solar system. *Geochimica et Cosmochimica Acta* 68: 2905–2923.
- Jaoul O., Froidevaux C., Durham W. B., and Michaut M. 1980, *Earth and Planet. Science Letters*, 47, 391–397.
- Jones A. P. and Nuth J. A. 2011. Dust destruction in the ISM: a re-evaluation of

dust lifetimes. *Astronomy and Astrophysics* 530: A44 (12pp).

- Kalampounias A. G., Nasikas N. K., and Papatheodorou G. N. 2009. Glass formation and structure in the MgSiO3–Mg2SiO4 pseudobinary system: From degraded networks to ioniclike glass. *The journal of Chemical Physics* 131: 14513–1–14513–8.
- Kawasaki N., Simon S. B., Grossman L., Sakamoto N., and Yurimoto H. 2018. Crystal growth and disequilibrium distribution of oxygen isotopes in an igneous CA-Al-rich inclusion from the Allende carbonaceous chondrite. *Geochimica et Cosmochimica Acta* 221: 318–341.
- Kemper F., Vriend W. J., and Tielens A. G. G. M. 2004. The absence of crystalline silicates in the diffuse interstellar medium. *The Astrophysical journal* 609: 826–837.
- Koike C., Imai Y., Chihara H., Suto H., Murata K., Tsuchiyama A., Tahicbana S., and Ohara S. 2010. Effects of forsterite grain shape in infrared spectra. *The Astrophysical journal* 709: 983–992.
- Krot A. N., Amelin Y., Bland P., Ciesla F. J., Connely J., Davis A. M., Huss G. R., Hutcheon I. D., Makida K., Nagashima K., Nyquist L. E., Russell S. S., Scott E. R. D., Thrane K., Yurimoto H., and Yin Q.-Z. (2009) Origin and chronology of chondritic components: A review. *Geochimica et Cosmochimica Acta* 73: 4963–4997.
- Kunihiro T., Nagashima K., and Yurimoto H. 2005. Microscopic oxygen isotopic homogeneity/heterogeneity in the matrix of the Vigarano CV3chondrite. *Geochimica et Cosmochimica Acta* 69: 763–773.
- Kuroda M., Tachibana S., Sakamoto N., Okumura S., Nakamura M., and Yurimoto H. 2018. Water diffusion in silica glass through pathways formed by hydroxyls. *American Mineralogist* 103: 412−417.
- Leitner J., Vollmer C., Hoppe P., and Zipfel J. 2012. Characterization of presolar material in the CR chondrite Northwest Africa 852. *The Astrophysical journal* 745:

38 (16pp).

- Lesher C. E., Hervig R. L., and Tinker D. 1996. Self diffusion of network formers (silicon and oxygen) in naturally occurring basaltic liquid. *Geochimica et Cosmochimica Acta* 60: 405–413.
- Liang Y., Richter F. M., Davis A. M., and Watson E. B. 1996. Diffusion in silicate melts: I. Self diffusion in $CaO-Al_2O_3-SiO_2$ at 1500°C and 1 GPa. *Geochimica et Cosmochimica Acta* 60: 4353–4367.
- Lodders K. 2003. Solar system abundances and condensation temperatures of the elements. *The Astrophysical journal* 591: 1220–1247.
- Lyons J. R. and Young E. D. 2005. CO self-shielding as the origin of oxygen isotope anomalies in the early solar nebula. *Nature* 435: 317–320.
- MacPherson G. J. (2003) Calcium-aluminum-rich inclusions in chondritic meteorites. In *Meteorites, comets, and planets* (Davis A. M. ed.) *Treatise on Geochemistry*, vol. 1. Oxford: Elsevier-Pergamon. pp201–246.
- MacPherson G. J., Simon S. B., Davis A. M., Grossman L., and Krot A. N. (2005) Calcium-aluminum-rich inclusions: Major unanswered questions. In *Chondrites and the Protoplanetary disk* (Krot A. N., Scott E. R. D., and Reipurth B. ed.) *ASP Conference Series*, vo. 1, San Francisco: Astronomical Society of the Pacific. pp225–250.
- McKeegan K. D., Leshin L. A., Russell S. S., and MacPherson G. J. 1996. *In situ* measurement of O isotopic anomalies in a Type B Allende CAI. *Meteoritics and Planetary Science* 31: A86–A87.
- McKeegan K. D., Aléon J., Bradley J., Brownlee D., Busemann H., Butterworth A., Chaussidon M., Fallon S., Floss C., Gilmour J., Gounelle M., Graham G., Guan Y., Heck P. R., Hoppe P., Hutcheon I. D., Huth J., Ishii H., Ito M., Jacobsen S. B., Kearsley A., Leshin L. A., Liu M-C., Lyon I., Marhas K., Marty B., Matrajt G., Meibom A., Messenger S., Mostefaoui S., Mukhopadhyay S., Nakamura-Messenger K., Nittler L., Palma R., Pepin R. O., Papanastassiou D. A.,

Robert F., Schlutter D., Snead C. J., Stadermann F. J., Stroud R., Tsou P., Westphal A., Young E. D., Ziegler K., Zimmermann L., and Zinner E. 2006. Isotopic compositions of cometary matter returned by Stardust. *Science* 314: 1724–1728.

- McKeegan K. D., Kallio A. P. A., Heber V. S., Jarzebinski G., Mao P. H., Coath C. D., Kunihiro T., Wiens R. C., Nordholt J. E., Moses Jr. R. W., Reisenfeld D. B., Jurewicz A. J. G., and Burnett D. S. 2011. The oxygen isotopic composition of the Sun inferred from capture solar wind. *Science* 332: 1528–1532.
- Mendybaev R. A., Richter F. M., and Davis A. M. 2006. Crystallization of melilite from CMAS-liquids and the formation of melilite mantle of Type B1 CAIs: Experimental simulations. *Geochimica et Cosmochimica Acta* 70: 2622–2642.
- Messenger S., Keller L. P., Stadermann F. J., Walker R. M., and Zinner E. 2003. Samples of stars beyond the solar system: Silicate grains in interplanetary dust. *Science* 300: 105–108.
- Murata K., Chihara H., Koike C., Takakura T., Imai Y., and Tsuchiyama A. 2009. Crystallization experiments on amorphous magnesium silicate. I. Estimation of the activation energy of enstatite crystallization. *The Astrophysical journal* 697: 836–842.
- Nagashima K., Krot A. N., and Yurimoto H. 2004. Stardust silicates form primitive meteorites. *Nature* 428: 921–924.
- Nakamura T., Noguchi T., Tsuchiyama A., Ushikubo T., Kita N. T., Valley J. W., Zolensky M. E., Kakazu Y., Sakamoto K., Mashio E., Uesugi K., and Nakano T. 2008. Chondrulelike objects in short-period comet 81P/Wild 2. *Science*, 321: 1664–1667.
- Nguyen A. and Zinner E. 2004. Discovery of ancient silicate stardust in a meteorite. *Science* 303: 1496–1499.
- Nguyen A. N., Berger E. L., Nakamura-Messenger K., Messanger S., and Keller L. P. 2017. Coordinated mineralogy and isotopic analyses of a cosmic symplectites

discovered in a comet 81P/Wild 2 sample. *Meteoritical and Planetary Science* 52, 2004–2016.

- Nuth J. A., Brearley A. J., and Scott E. R. D. 2005. Microcrystals and amorphous materials in comets and primitive meteorites: Keys to understanding processes in the early Solar System. In *Workshop on Chondrites and the Protoplanetary disk* (Krot A. N., Scott E. R. D., and Reipurth B. ed.), Astronomical Society of the Pacific Conference Series, vol. 341, pp675–700.
- Oishi Y., Terai R., and Ueda H. 1974. Oxygen diffusion in liquid silicates and relation to their viscosity. In *Mass Transport in Ceramics and relation to their viscosity* (Cooper A. R. and Heuer A. H. ed.) Premium Press. pp297–310.
- Pascucci I. and Tachibana S. 2010. The clearing of protoplanetary disks and of the proto-solar nebul. In *Protoplanetary dust: Astrophysical and cosmochemical perspectives* (Apai D. and Lauretta D. S ed.), 1st ed., New York: Cambridge University Press. pp263–298.
- Paque J. M., Lofgren G. E., and Le L. 2000. Crystallization of calciumaluminum-rich inclusions: Experimental studies on the effects of repeated heating events. *Meteoritics and Planetary Science* 35: 363–371.
- Pontoppidan K. M. and Brearley A. J. 2010. Dust particle size evolution. In *Protoplanetary dust: Astrophysical and cosmochemical perspectives* (Apai D. and Lauretta D. S ed.), 1st ed., New York: Cambridge University Press. pp191–229.
- Ratzka Th., Leinert Ch., Henning Th., Bouwman J., Dullemond C. P. and Jaffe W. 2007. High special resolution mid-infrared observations of the low-mass young star TW Hydrae. *Astronomy and Astrophysics* 471, 173–185.
- Ryerson F. J. and McKeegan K. D. 1994. Determination of oxygen self-diffusion in åkermanite, anorthite, diopside, and spinel: Implications for oxygen isotopic anomalies and the thermal history of Ca-Al-rich inclusions. *Geochimica et Cosmochimica Acta* 58: 3713–3734.
- Ryerson F. J., Durham W. B., Cherniak D. J., and Lanford W. A. 1989. Oxygen

diffusion in olivine: Effect of oxygen fugacity and implications for creep. Journal of geophysical research 94: 4105–4118.

- Sakamoto N., Seto Y., Itoh S., Kuramoto K., Fujino K., Nagashima K., Krot A. N., and Yurimoto H. 2007. Remnants of the early solar system water enriched din heavy oxygen isotopes. *Science* 317: 231–233.
- Seto Y., Sakamoto N., Fujino K., Kaito T. Oikawa T., and Yurimot H. 2008. Mineralogical characterization of a unique material having heavy oxygen isotope anomaly in matrix of the primitive carbonaceous chondrite Acfer 094. *Geochimica et Cosmochimica Acta*, 72, 2723–2734.
- Simon J. I., Cuzzi J. N., McCain K. A., Cato M. J., Christoffersen P. A., Fisher K. R., Srinivasan P., Tait A. W., Olson D. M., and Scargle J. D. 2018. Particle size distributions in chondritic meteorites: Evidence for pre-planetesimal histories. *Earth and Planetary Science Letters* 494: 69–82.
- Stolper E. 1982. Crystallization sequences of Ca-Al-rich inclusions from Allende: An experimental study. *Geochimica et Cosmochimica Acta* 46: 2159–2180.
- Stolper E. and Paque J. M. 1986. Crystallization sequences of Ca-Al-rich inclusions from Allende: The effects of cooling rate and maximum temperature. *Geochimica et Cosmochimica Acta* 50: 1785–1806.
- Tachibana S., Nagahara H., Ozawa K., Ikeda Y., Nomura R., Tatsumi K., and Joh Y. 2011. Kinetic condensation and evaporation of metallic iron and implications for metallic iron dust formation. *The Astrophysical journal* 736: 16 (8pp).
- van Boekel R., Min M., Waters L. B. F. M., de Koter A., Dominik C., van den Ancker M. E., and Bouwman J. 2005. A 10 μm spectroscopic survey of Herbig Ae star disks: Grain growth and crystallization. *Astronomy and Astrophysics*, 437, 189–208.
- Vollmer C., Hoppe P., and Brenker F. E. 2013. Transmission electron microscopy of Al-rich silicate stardust from asymptotic giant branch stars. *The Astrophysical journal* 769: 61 (8pp).

- Waters L. B. F. M., Molster F. J., de Jong T., Beintema D. A., Waelkens C., Boogert A. C. A., Boxhoorn D. R., de Graauw Th., Drapatz S., Feuchtgruber H., Genzel R., Helmich F. P., Heras A. M., Huygen R., Izumiura H., Justtanont K., Kester D. J. M., Kunze D., Lahuis F., Lamers H. J. G. L. M., Leech K. J., Loup C., Lutz D., Morris P. W., Price S. D., Roelfsema P. R., Salama A., Schaeidt S. G., Tielens A. G. G. M., Trams N. R., Valentijn E. A., Vandenbussche B., van den Ancker M. E., van Dishoeck E. F., van Winckel H., Wesselius P. R., and Young E. T. 1996. Mineralogy of oxygen-rich dust shells. *Astronomy and Astrophysics* 315: L361–L364.
- Wark D. 1979. Birth of the presolar nebula: The sequence of condensation revealed in the Allende meteorite. *Astrophysics and Space Science* 65: 275–295.
- Wasson J. T., Yurimoto H., and Russell S. S. 2001. ^{16}O-rich melilite in CO3.0 chondrites: Possible formation of common, 16O-poor melilite by aqueous alteration. *Geochimica et Cosmochimica Acta* 65: 4539–4549.
- Wood J. A. and Morfill G. E. 1988. A review of solar nebula mode. In *Meteorites and the Early Solar System* (Kerridge J. F. and Matthews M. S ed.), Tucson, AZ: University of Arizona Press. pp329–347.
- Yamamoto D. and Tachibana S. 2018. Water vapor pressure dependence of crystallization kinetics of amorphous forsterite. *American Chemical Society Earth and Space Chemistry* 2: 778–786.
- Yoshitake M., Koide Y., and Yurimoto H. 2005. Correlations between oxygen-isotopic composition and petrologic setting in a coarse-grained Ca, Al-rich inclusion. *Geochimica et Cosmochimica Acta* 69: 2663–2674.
- Yu Y., Hewins R. H., Clayton R. N., and Mayeda T. K. 1995. Experimental study of high temperature oxygen isotope exchange during chondrule formation. *Geochimica et Cosmochimica Acta* 59: 2095–2104.
- Yurimoto H., Nagasawa H., Mori Y., and Matsubayashi O. 1994. Micro-distribution of oxygen isotopes in a refractory inclusion from the Allende

meteorite. *Earth and Planetary Science Letters* 128: 47–53.

- Yurimoto H., Ito M., and Nagasawa H. 1998. Oxygen isotope exchange between refractory inclusion in Allende and solar nebula gas. *Science* 282: 1874–1877.
- Yurimoto H. and Kuramoto K. 2004. Molecular cloud origin for the oxygen isotope heterogeneity in the solar system. *Science* 305: 1763–1766.
- Zinner E. 2014. Presolar grains. In *Treatise on Geochemistry*, 2nd ed., vol. 1.4, edited by Holland H. D. and Turekian K. K.; vol. edited by Davis A. M. Oxford and San Diego: Elsevier. pp181–213.